Self-sustained Multicentennial Oscillation of the Atlantic Meridional Overturning Circulation in Two-hemisphere Box Models

Xiangying Zhou, Kunpeng Yang, Haijun Yang*

Department of Atmospheric and Oceanic Sciences and Key Laboratory of Polar Atmosphere-ocean-ice System for Weather and Climate of Ministry of Education, Fudan University, Shanghai, 200438, China

Climate Dynamics

1st submission, March 7, 2025

Corresponding author: Haijun Yang, yanghj@fudan.edu.cn

ABSTRACT

Self-sustained multicentennial variability of the Atlantic Meridional Overturning Circulation (AMOC) has been previously demonstrated in one-hemisphere box models. In this study, we extend our earlier work by developing a two-hemisphere box model that incorporates both thermohaline and wind-driven components. Our analysis reveals that a robust, weakly damped multicentennial eigenmode persists in the two-hemisphere framework, with the salinity advection feedback in the North Atlantic remaining the dominant control mechanism, while the South Atlantic plays a minor role. Compared to the one-hemisphere model, the self-sustained multicentennial oscillation in the two-hemisphere box model is much easier to occur and less sensitivity to changes in basin geometry. Moreover, the inclusion of wind-driven circulation acts to weaken the oscillation amplitude, with negligible impact on the oscillation period. We further demonstrate that the AMOC itself is a necessary and sufficient condition for the multicentennial oscillation, as the mode vanishes when the AMOC is shut down. Finally, stochastic freshwater forcing can excite a sustained oscillation, confirming that the multicentennial mode is intrinsic to the AMOC. We also identify a damped millennial oscillatory mode that deserves further investigation, as it may provide clues to understanding

KEYWORDS: Atlantic meridional overturning circulation, Box model, Self-sustained multicentennial oscillation, Thermohaline circulation, Wind-driven circulation

1. Introduction

Through analyses of proxy data and model simulation outputs, researchers have identified multicentennial climate variability (Askjær et al. 2022; Moffa‐Sánchez et al. 2019; Wanner et al. 2008), which may have influenced the course of human history to some extent. It is widely recognized that the low-frequency climate variability beyond decadal timescale is linked to ocean circulations, particularly the Atlantic Meridional Overturning Circulation (AMOC) (Srokosz et al. 2012; Stocker and Mysak 1992). This association is supported by significant signals of multicentennial variability observed in proxy data within the North Atlantic region (Askjær et al. 2022; Moffa‐Sánchez et al. 2019; Sejrup et al. 2011). Moreover, numerical model simulations have consistently indicated the existence of multicentennial variability of the AMOC (e.g., Delworth and Zeng 2012; Jiang et al. 2021; Martin et al. 2013, 2015; Meccia et al. 2022; Mehling et al. 2023; Park and Latif 2008), which may induce multicentennial variability of the Earth's climate system.

Some studies suggested that the multicentennial variability of the AMOC is driven by external natural forcing of the climate system (e.g., Weber et al. 2004), while others focused on internal processes within the ocean itself (e.g., Cao et al. 2023; Delworth and Zeng 2012; te Raa and Dijkstra 2003; Winton and Sarachik 1993). In the studies supporting this variability arose from an internal process, most researchers agreed that salinity anomalies in the North Atlantic Deep Water (NADW) formation region is an important factor (e.g., Cao et al. 2023; Delworth and Zeng 2012; Mikolajewicz and Maier-Reimer 1990; Mysak et al. 1993; Sévellec et al. 2006). Salinity anomalies in the NADW formation region can be generated by the positive salinity advection feedback, i.e., an enhanced AMOC will make the subpolar ocean more saline and thus denser, which in turn reinforces the AMOC.

Specific processes responsible for generating and maintaining the multicentennial variability of the AMOC can be more clearly investigated in simple theoretical models. Griffies and Tziperman (1995) realized a stochastically forced AMOC oscillation in their four-box model but the time scale is of multidecadal. Self-sustained multidecadal oscillations of the AMOC can also be realized in box models (Rivin and Tziperman 1997; Wei and Zhang 2022). Roebber (1995) realized a multicentennial oscillation of the AMOC in a three-box ocean model forced by chaotic atmosphere. Sévellec et al. (2006) found self-sustained multicentennial oscillations of the AMOC in a variety of models, including a two-dimensional ocean model and a theoretical loop model. Multicentennial oscillations of the AMOC are also found in two-hemisphere three-box model (Lucarini and Stone 2005a, 2005b; Scott et al. 1999).

Recently, Li and Yang (2022) (hereafter LY22) identified a multicentennial eigenmode of the AMOC in a one-hemisphere box model including only saline processes, which can exhibit self-sustained multicentennial oscillation (multicentennial oscillation) in the presence of enhanced vertical mixing in the NADW formation region. Yang et al. (2024) (hereafter YYL24) expanded the work of LY22 by incorporating both thermal and saline processes in their one-hemisphere box model. Their findings indicated that the thermal processes can stabilize the oscillatory system and shorten the oscillation period; however, the fundamental behavior of the oscillation system is still controlled by the saline processes. Besides the internal nonlinear vertical mixing (LY22), the self-sustained AMOC multicentennial oscillation can also be maintained by a weak nonlinear relationship between the AMOC strength and the meridional density gradient.

This study is a subsequent investigation in our ongoing series of theoretical studies on the AMOC multicentennial oscillation. In this work, we expand the one-hemisphere box model developed in LY22 and YYL24 to a two-hemisphere box model. Additionally, we incorporate both the thermohaline and wind-driven components of the AMOC, allowing for a comprehensive examination of the influence of the wind-driven circulation, particularly the subtropical cell, on the low-frequency variability of the AMOC. While previous research demonstrated the significance of the wind-driven circulation in influencing the AMOC (Gao and Yu 2008; Guan and Huang 2008; Klockmann et al. 2020; Pasquero and Tziperman 2004; Sun et al. 2021), its specific role in the AMOC multicentennial oscillation remains an area of further investigation. Therefore, one of objectives of this paper is to address a research gap by conducting an in-depth analysis of the impact of the wind-driven subtropical cell, on the multicentennial oscillation.

Results in this paper show that the multicentennial eigenmode also exists in the two-hemisphere box model, which is less affected by the model parameters compared to those in the one-hemisphere box model. Adding antisymmetric transports from the equator to polar oceans in the two-hemisphere box model, i.e., including the effect of the wind-driven mass transport, can stabilize the oscillation, reduce the oscillatory amplitude, and prolong the oscillatory period slightly. In this paper, we depict the inter-hemispheric nature of the AMOC, enhancing our understanding of the multicentennial oscillation and enriching the theory beyond the limitations of the single-hemisphere model and the thermohaline circulation.

This paper is organized as follows. In section 2, a two-hemisphere box model with only salinity equations (hereafter the 6S model) is introduced, and eigenvalues of this linear system are analyzed. In section 3, we realize a self-sustained multicentennial oscillation of the AMOC in the 6S model and investigate the role of the subpolar South Atlantic. In section 4, temperature equations and wind-driven subtropical cell are incorporated, and their effects on the multicentennial oscillation are analyzed. In section 5, stochastic forcing is used to force the box model and the sustained multicentennial oscillation is obtained, which further prove that the multicentennial mode is an eigenmode of the thermohaline circulation. Summary and discussion are presented in section 6. Pertinent background information obtained from two coupled models, and the derivation of theoretical formulas for several simplified two-hemisphere models are included in Appendices.

2. Two-hemisphere box model

a. Salinity-only thermohaline model

The two-hemisphere box model used here consists of six ocean boxes (Fig. 1). With a zonal width of 5200 km and a meridional extent of 140°, the model domain spans two hemispheres and is separated into three zones by latitudes 45°N and 30°S. The AMOC is clockwise in the box model, sinking in the subpolar North Atlantic and rising in the subpolar South Atlantic.

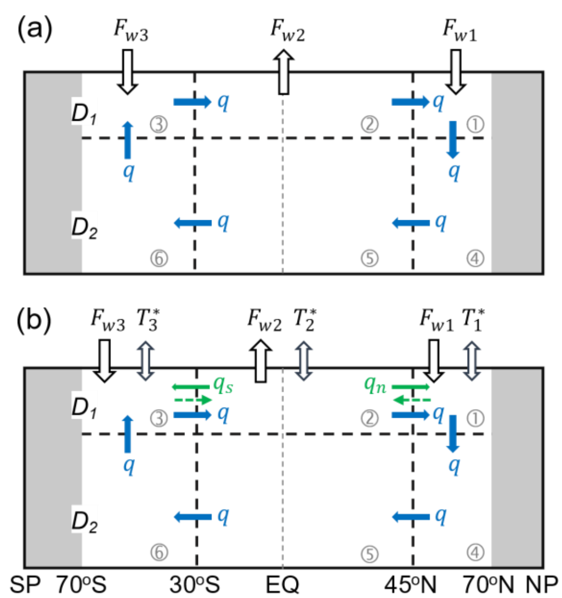

FIG. 1. Schematic diagrams of ocean box models. (a) The 6-box salinity-only model (6S model); and (b) the 6-box temperature-salinity model (6TS model) with the wind-driven circulation included. The circled numbers (e.g.,

① and ②) denote the ocean boxes. Boxes 1 and 4 represent the upper and lower subpolar North Atlantic, respectively; boxes 2 and 5 represent the upper and lower tropical oceans, respectively; boxes 3 and 6 represent the upper and lower subpolar South Atlantic, respectively. D_1 and D_2 are the depths of the upper and lower oceans, respectively. F_{w1}, F_{w2}, and F_{w3} are the virtual salt fluxes into boxes 1-3, representing surface freshwater fluxes in reality. T_1^*, T_2^*, and T_3^* are the restoring temperatures of boxes 1-3. q represents the AMOC. q_n and q_s are northward and southward transports by the wind-driven circulation, respectively. The green solid and dashed arrows represent poleward and equatorward wind-driven transports, all occurring in the upper ocean and having the same magnitude.

The salinity equations in the 6S model (Fig. 1a) can be written as follows,

$$V_1\dot{S_1} = q(S_2 - S_1) + F_{w1} \tag{1a}$$

$$V_2\dot{S_2} = q(S_3 - S_2) + F_{w2} \tag{1b}$$

$$V_3\dot{S_3} = q(S_6 - S_3) + F_{w3} \tag{1c}$$

$$V_4\dot{S_4} = q(S_1 - S_4) \tag{1d}$$

$$V_5\dot{S_5} = q(S_4 - S_5) \tag{1e}$$

$$V_6\dot{S_6} = q(S_5 - S_6) \tag{1f}$$

where V_i and S_i are the volume and salinity of box i, and q is the AMOC strength. F_{wi} is the virtual salt flux for the upper boxes, representing surface freshwater fluxes across corresponding boxes.

The equilibrium solutions of Eq. (1) are,

$$\bar{q}(\bar{S_1} - \bar{S_2}) = F_{w1} \tag{2a}$$

$$\bar{q}(\bar{S_2} - \bar{S_3}) = F_{w2} \tag{2b}$$

$$\bar{q}(\bar{S_3} - \bar{S_1}) = F_{w3} \tag{2c}$$

$$\bar{S_1} = \bar{S_4} = \bar{S_5} = \bar{S_6} \tag{2d}$$

$$F_{w1} + F_{w2} + F_{w3} = 0 \tag{2e}$$

where, $\bar{q}$ is set to 24 Sv. F_{w1}, F_{w2}, and F_{w3} are set to -7.2×10^7, 7.44×10^7, and -0.24×10^7 psu m^3 s^{-1}, which give $\bar{S_1} = 33.9$, $\bar{S_2} = 36.9$, and $\bar{S_3} = 33.8$ psu, respectively. The model is tuned so that its equilibria nearly agree with the results of the two coupled models examined in Appendix A. Other parameters used in the 6S model are listed in Table 1.

TABLE 1. Standard values of parameters and equilibria used in this study. WDC is an abbreviation of wind-driven circulation.

Symbol	Physical meaning	Value with units

L_1, L_2, L_3, L	Meridional scales of northern subpolar, tropical, southern subpolar ocean boxes, and the total scale	25°, 75°, 40°, 140°
D_1, D_2, D	Thicknesses of the upper, deeper, and their sum	1000, 3000, 4000 m
V_1	Volume of box 1	1.443×10^{16} m^3 (for 5200 km wide)
V_2, V_3, V_4, V_5, V_6	Volumes of boxes 2, 3, 4, 5, and 6	$3V_1$, $1.6V_1$, $3V_1$, $9V_1$, $4.8V_1$
γ	Restoring coefficient of boxes 1, 2, and 3	3.171×10^{-8} s^{-1}
T_1^*, T_2^*, T_3^*	Restoring temperatures of boxes 1, 2, and 3	3.7, 24.5, 7.7 °C (without WDC)
		3.4, 24.6, 7.6 °C (with WDC)
F_{w1}, F_{w2}, F_{w3}	Surface virtual salt fluxes into boxes 1, 2, and 3	-7.20×10^7, 7.44×10^7, -0.24×10^7 psu m^3 s^{-1} (without WDC)
		-8.97×10^7, 10.79×10^7, -1.82×10^7 psu m^3 s^{-1} (with WDC)
λ	Linear closure coefficient	21.3 Sv kg^{-1} m^3
α	Thermal expansion coefficient	1.468×10^{-4} $°C^{-1}$
β	Saline contraction coefficient	7.61×10^{-4} psu^{-1}
ρ_0	Reference seawater density	1.0×10^3 kg m^{-3}
k_n, k_s	Wind-driven advection coefficients for the NA and SA	0.307 Sv $°C^{-1}$
$\bar{q}$	Equilibrium AMOC strength	24 Sv (10^6 m^3 s^{-1})
$\overline{q_n}, \overline{q_s}$	Equilibrium WDC transports	5.9, 5.1 Sv
$\bar{T}_1, \bar{T}_2, \bar{T}_3, \bar{T}_4, \bar{T}_5, \bar{T}_6$	Equilibrium temperatures of six boxes	4.9, 24.2, 7.6, 4.9, 4.9, 4.9 °C
$\bar{S}_1, \bar{S}_2, \bar{S}_3, \bar{S}_4, \bar{S}_5, \bar{S}_6$	Equilibrium salinities of six boxes	33.9, 36.9, 33.8, 33.9, 33.9, 33.9 psu

Eq. (1) can be linearized as follows,

$$V_1\dot{S}_1' = \bar{q}(S_2' - S_1') + q'(\bar{S}_2 - \bar{S}_1) \tag{3a}$$

$$V_2\dot{S}_2' = \bar{q}(S_3' - S_2') + q'(\bar{S}_3 - \bar{S}_2) \tag{3b}$$

$$V_3\dot{S}_3' = \bar{q}(S_6' - S_3') + q'(\bar{S}_6 - \bar{S}_3) \tag{3c}$$

$$V_4\dot{S}_4' = \bar{q}(S_1' - S_4') \tag{3d}$$

$$V_5\dot{S}_5' = \bar{q}(S_4' - S_5') \tag{3e}$$

$$V_6\dot{S}_6' = \bar{q}(S_5' - S_6') \tag{3f}$$

In Eq. (3), the AMOC anomaly q' is parameterized as a linear function of density difference between two subpolar boxes. This linear relation is validated in two coupled models (CESM1.0 and EC-Earth3-Veg-LR; Figs. A1 and A2 in Appendix A), and can be expressed as follows,

$$q = \bar{q} + q' = \bar{q} + \lambda \Delta\rho' \tag{4}$$

$$\Delta\rho' = \rho_0\beta[\delta(S_1' - S_3') + (1-\delta)(S_4' - S_6')]$$

and

$$\delta = \frac{V_1}{V_1+V_4} = \frac{V_3}{V_3+V_6} = \frac{D_1}{D} \tag{5}$$

b. Linear stability analysis

Eigenvalues of the 6S model can be obtained numerically. Using the parameters in Table 1, we obtain two pairs of conjugate eigenvalues: a weakly unstable multicentennial mode (ω = 0.34 ± 5.85*i*) and a strongly damped millennial mode (ω = –8.34 ± 1.12*i*) (Table 2), respectively. The system has two additional eigenvalues: 0 and –19.19, corresponding to a zero mode (i.e., the equilibrium climate) and a purely damped mode with an e-folding time of about 20 years.

TABLE 2. Eigenvalues (ω; 10^{-10} s^{-1}) in two-hemisphere box model. Particular parameters are k_n = k_s = 0, λ = 24.6 Sv kg^{-1} m^3, $\bar{q}$ = 24 Sv in the 6TS_THC model, k_n = k_s = 0.30 Sv °C^{-1}, λ = 31.3 Sv kg^{-1} m^3, $\bar{q}$ = 24 Sv in the 6TS_THC+WDC model, and k_n = k_s = 0.30 Sv °C^{-1}, λ = 0, $\bar{q}$ = 0 in the 6TS_WDC model.

	6S	6TS			Physical meaning
	THC	THC	THC+WDC	WDC	
In 10^{-10} s^{-1}	0.34±5.85*i*	0.58±6.05*i*	0.43±5.81*i*	/	Oscillatory mode
In Year	933±340*i*	547±329*i*	737±343*i*	/	
In 10^{-10} s^{-1}	–8.34±1.12*i*	–8.17±0.73*i*	/	/	Oscillatory mode
In Year	–38±1779*i*	–39±2729*i*	/	/	
In 10^{-10} s^{-1}	0	0	0	0	Zero mode

	–19.2	–348, –328, –320, –19.4, –5.6, –3.9, –1.6	–363, –337, –320, –23.3, –14.1, –6.2, –5.7, –4.0, –1.5	–331, –324, –317, –7.2, –3.3	Damped mode

The multicentennial mode has a period of about 340 years and an e-folding time of about 930 years when λ = 21.3 Sv kg^{-1} m^3, indicating a weakly unstable oscillation. The multicentennial mode depends closely on the closure parameter λ (Fig. 2). The real part of the eigenvalue [Re(ω)] increases with λ (Fig. 2a), while the imaginary part [Im(ω)] has a maximum value when λ = 21.3 Sv kg^{-1} m^3 (Fig. 2b). This dependence is similar to that in the one-hemisphere box model of LY22 and YYL24. Eigenvalues under $\lambda < 0$ do not have any physical meaning and are not plotted in Fig. 2.

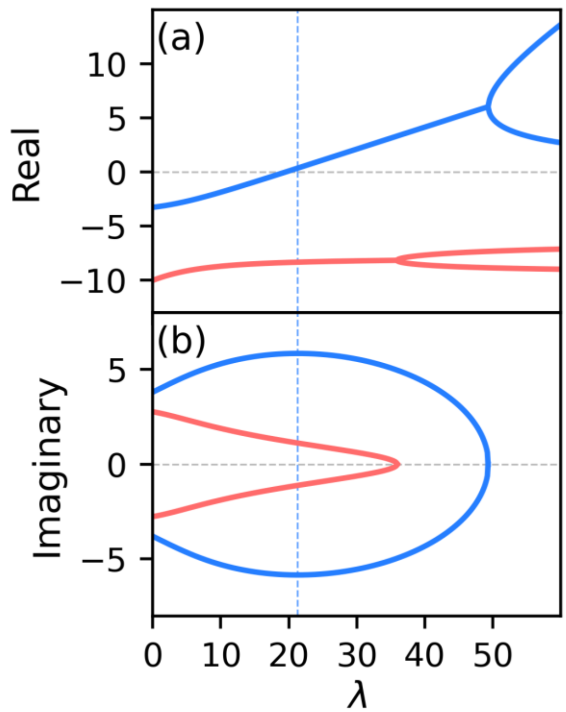

FIG. 2. Dependences of (a) damping rate [Re(ω)] and (b) frequency [Im(ω)] of the multicentennial (blue curves) and millennial (red curves) oscillatory modes on λ (units: Sv kg^{-1} m^3) in the 6S model using the parameters in Table 1. The vertical dashed blue line corresponds to λ = 21.3 Sv kg^{-1} m^3 when Im(ω) of the multicentennial mode reaches the maximum. The units of the ordinate are 10^{-10} s^{-1}.

The millennial mode identified here was absent in the one-hemisphere model. The millennial mode has a period about 1800 years and a much shorter e-folding time of about –40 years when λ = 21.3 Sv kg^{-1} m^3. With the increase of λ, Im(ω) decreases and Re(ω) is roughly unchanged (Red curves in Figs. 2a, b). Note that Re(ω) is always negative and much smaller than Im(ω), suggesting that this millennial mode is always a strongly damped mode. We are not sure whether this mode is physically meaningful and in-depth investigations on this mode will be conducted in our future study.

3. Robust multicentennial oscillations

a. Self-sustained oscillations

In studies employing theoretical models, sustained oscillations can arise from either external forcing or intrinsic nonlinearity (Griffies and Tziperman 1995; Rivin and Tziperman 1997; LY22; YYL24). A self-sustained AMOC oscillation can be realized by convection (Sévellec et al. (2006)) or enhanced vertical mixing (LY22) in the subpolar North Atlantic, or by introducing a nonlinear relationship between the AMOC strength and meridional density difference (Rivin and Tziperman 1997; YYL24). Here, we simply adopt the approach in LY22.

Adding enhanced vertical mixing between the upper and lower subpolar oceans (boxes 1 and 4) in the 6S model, Eqs. (3a) and (3d) become,

$$V_1\dot{S}_1' = \bar{q}(S_2' - S_1') + q'(\overline{S_2} - \overline{S_1}) - k_m(S_1' - S_4') \tag{6a}$$

$$V_4\dot{S}_4' = \bar{q}(S_1' - S_4') + k_m(S_1' - S_4') \tag{6b}$$

$$k_m = \kappa {q'}^2 \tag{6c}$$

where κ is a positive constant and is set to 10^{-3} m^{-3} s in this paper. As a result, k_m is always positive and represents a process that always transfers the salinity anomaly of upper ocean downward to lower ocean, no matter whether the AMOC is stronger or weaker than usual. The physics of the enhanced subpolar vertical mixing process was discussed in detail in LY22.

Figure 3 shows the results through numerical integration of the 6S model [Eq. (3)], and the results when enhanced vertical mixing is introduced in the subpolar North Atlantic [Eqs. (3) and (6)]. The integration starts from an initial salinity perturbation in the subpolar North Atlantic (S_1' = –0.02 psu). The forward fourth-order Runge-Kutta method is used to solve the equations. The integration time step is one year and the total integration length is longer than 10000 years. Given the velocity closure parameter λ = 21.3 Sv kg^{-1} m^3, the time series of salinity anomalies show oscillations with periods about 340 years and gradually enhancing amplitude (dashed grey curve in Fig. 3a), which are predicted by the eigenvalues discussed in section 2. After adding the enhanced mixing in the subpolar

North Atlantic, the unstable oscillation becomes a self-sustained oscillation with a limited amplitude (solid curves in Fig. 3a).

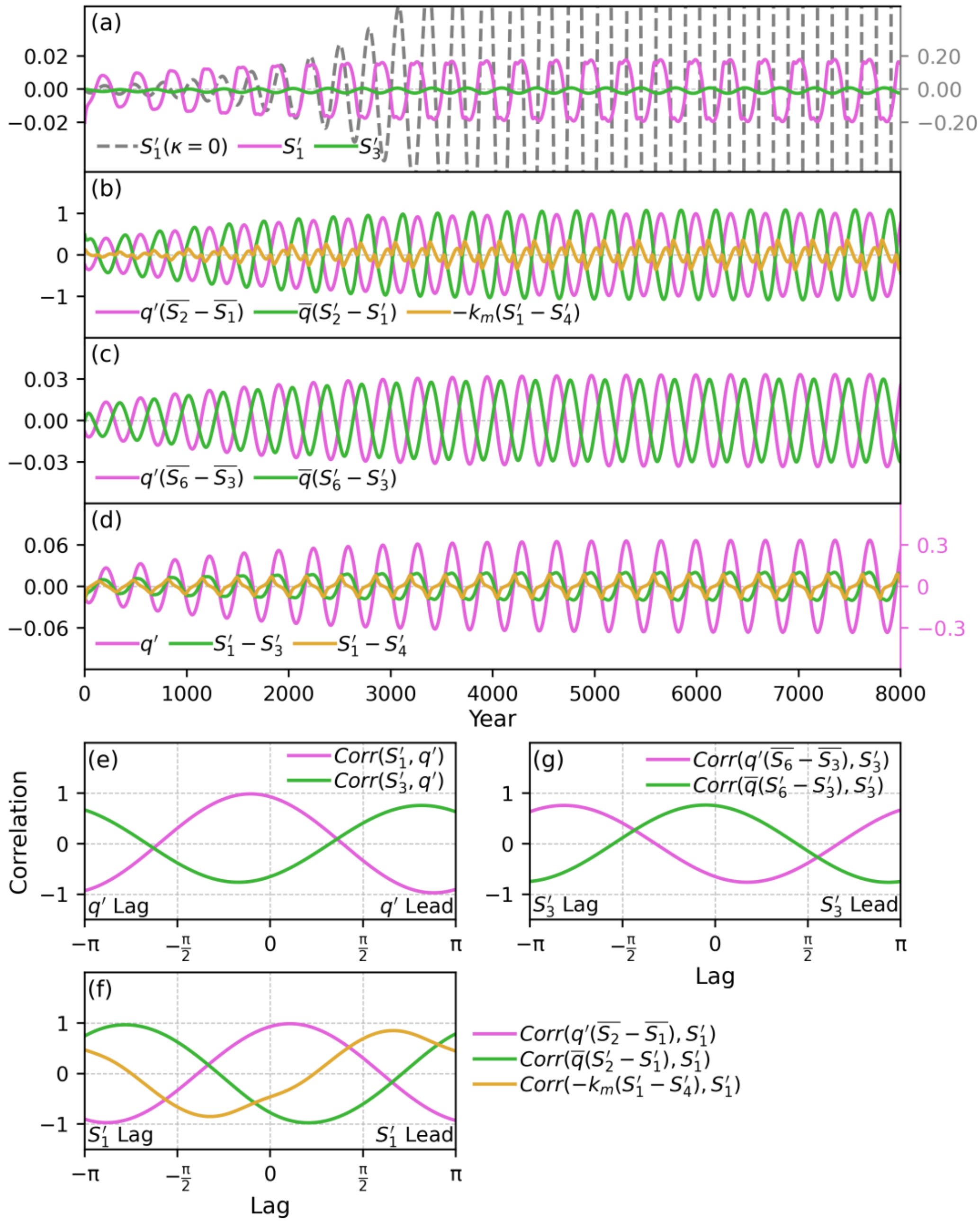

FIG. 3. (a) Unstable oscillation of S_1' (dashed curve; units: psu) in the 6S model without enhanced vertical mixing ($\kappa = 0$) in the subpolar North Atlantic; self-sustained oscillations of S_1' and S_3' with the enhanced vertical mixing. (b)-(c) Self-sustained oscillations of salinity terms (units: Sv psu) in the 6S model with the enhanced vertical mixing in the subpolar North Atlantic: (b) $q'(\overline{S}_2 - \overline{S}_1)$, $\overline{q}(S_2' - S_1')$, and $-k_m(S_1' - S_4')$, which are on the right-hand side of Eq. (6a), (c) $q'(\overline{S}_1 - \overline{S}_3)$ and $\overline{q}(S_6' - S_3')$, which are on the right-hand side of Eq. (3c). (d) Time series of q' (units: Sv), $S_1' - S_3'$, and $S_1' - S_4'$. (e) Lead-lag correlation coefficients of q' with S_1' and S_3'. For negative lags, salinity anomaly leads. (f) Lead-lag correlation coefficients between S_1' and individual salinity terms on the

right-hand side of Eq. (6a), which are $q'(\overline{S_2} - \overline{S_1})$, $\overline{q}(S_2' - S_1')$, and $-k_m(S_1' - S_4')$. Salinity terms lead for negative lags, salinity terms lead. (g) Lead-lag correlation coefficients between S_3' and individual salinity terms on the right-hand side of Eq. (3c), which are $q'(\overline{S_1} - \overline{S_3})$ and $\overline{q}(S_6' - S_3')$. For negative lags, salinity terms lead. Legends for the curves are labeled on the respective panels.

Physical processes contributing to the multicentennial oscillation of the AMOC are examined here. q' is roughly in phase with S_1' and out of phase with S_3' (Fig. 3e); thus, q' synchronizes with $S_1' - S_3'$ (Fig. 3d). Compared to S_3', S_1' has a larger amplitude and dominates q'. The growth of S_1' depends on three processes, as shown in Eq. (6a). The perturbation advection $q'(\overline{S_2} - \overline{S_1})$ has a positive correlation with S_1', which leads to positive feedback between S_1' and q'. The mean advection $[\overline{q}(S_2' - S_1')]$ and enhanced vertical mixing $[-k_m(S_1' - S_4')]$ lead to negative feedback for q' because S_1' is negatively correlated to the change of itself. The lead-lag correlation in Fig. 3f clearly illustrates the feedbacks of these terms with S_1'. Supposing that there is a positive anomaly in q' initially, the positive perturbation advection $[q'(\overline{S_2} - \overline{S_1})]$ first contributes to the growth of S_1' and further increases q'. Then, the growing S_1' enhances the negative feedback through strengthening mean advection $[\overline{q}(S_2' - S_1')]$ and vertical mixing $[-k_m(S_1' - S_4')]$, which in turn restricts the growth of S_1' and ocean stratification $(S_1' - S_4')$ (Fig. 3d). As a result, the further growth of q' is restrained and the oscillation is stabilized. These processes were deliberated in our previous studies using the one-hemisphere box model (LY22; YYL24).

The subpolar South Atlantic plays the secondary role in regulating the multicentennial oscillation because of the smaller amplitude of S_3' (Fig. 3a). For S_3', both the perturbation advection $[q'(\overline{S_6} - \overline{S_3})]$ and mean advection $[\overline{q}(S_6' - S_3')]$ in Eq. (3c) give negative feedbacks (Fig. 3g). However, for q', these two processes play as negative feedback and positive feedback, respectively. Starting with a positive perturbation of q', the perturbation advection $[q'(\overline{S_6} - \overline{S_3})]$ contributes to the growth of S_3' (Fig. 3f), which tends to reduce q' (Fig. 3e). Physically, it can be understood as that positive $q'(\overline{S_6} - \overline{S_3})$ removes the freshwater from the subpolar South Atlantic and increase the salinity over there. As a result, the ascending of the AMOC in the subpolar South Atlantic is restrained, so that the AMOC development in the North Atlantic is also restrained eventually. In addition, growing S_3' leads to the decline of mean advection $[\overline{q}(S_6' - S_3')]$ (Fig. 3g), which in turn restricts the growth of S_3' but promotes q'. Since q' is mainly controlled by $(S_1' - S_3')$ [Eq. (5)], the smaller amplitude of S_3' than that of S_1' (Fig. 3a) suggests a minor role of the Southern Ocean in the multicentennial oscillation of the AMOC.

b. Sensitivity of multicentennial oscillation mode to basin geometry

The model basin geometry can affect both the e-folding time and period of the multicentennial oscillation (Fig. 4). Keeping $\bar{q}$, $\overline{F_w}$, V, and λ unchanged as in Table 1, the dependence of the multicentennial eigenmode on the volumes of the subpolar North Atlantic ($V_1 + V_4$) and the global upper ocean ($V_1 + V_2 + V_3$) is exhibited in Figs. 4a, b. The influence of the volume of the subpolar South Atlantic ($V_3 + V_6$) on the multicentennial mode is analyzed in Figs. 4c, d. The blue star denotes the mode under the standard parameters in Table 1. Similar to Fig. 9 in LY22, the stability thresholds of the 6S and 5S (Appendix B, Fig. B1) models are marked by the pink and purple curves, respectively, which divide the phase space into three regions with different stability: the oscillations are decayed in region 1, self-sustained in region 2 when including enhanced vertical mixing, and unstable in region 3 regardless of the presence of enhanced vertical mixing or not.

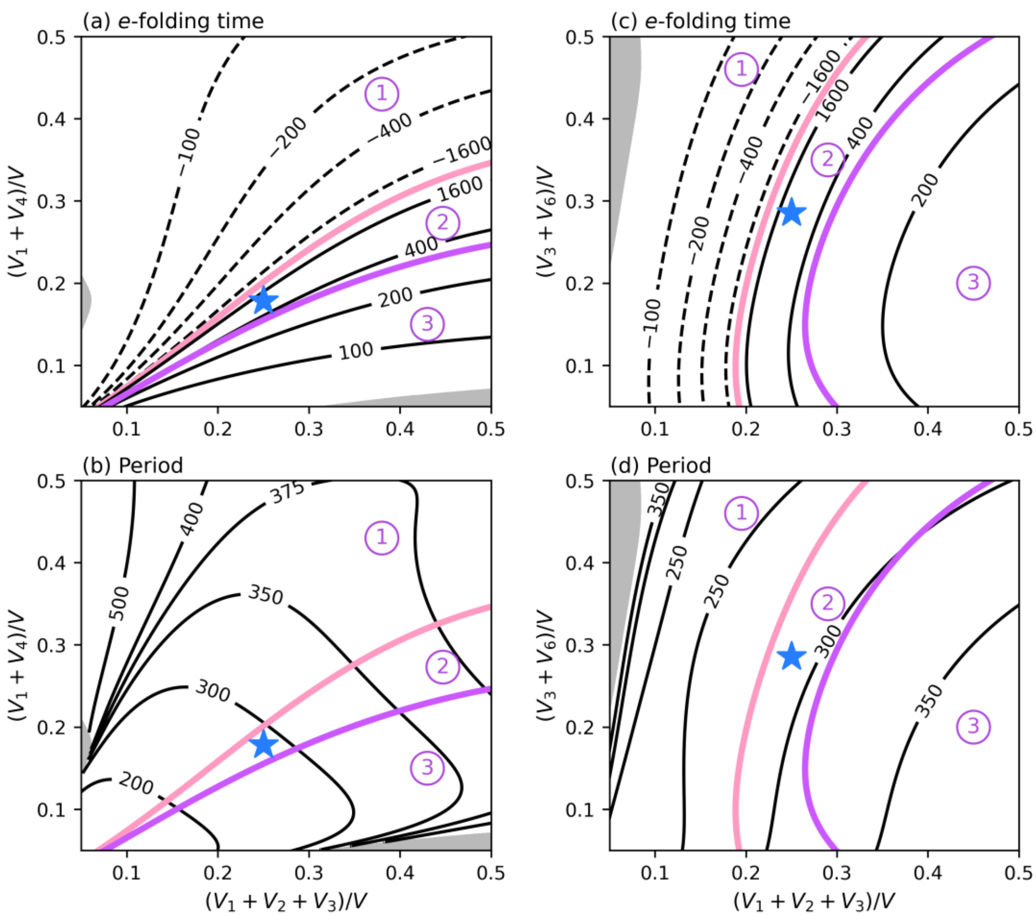

FIG. 4. Sensitivity of (a) e-folding time (units: year) and (b) period (units: year) of multicentennial oscillatory modes to model geometry in the 6S model. The abscissa and ordinate represent the volume fractions of the upper ocean $(V_1 + V_2 + V_3)/V$ and the northern subpolar ocean $(V_1 + V_4)/V$, respectively, where V is the total ocean volume. The solid pink and purple curves are the stability thresholds of the 6S and 5S models, respectively, dividing the contour plots into three regions. The oscillatory modes are decayed in region 1, self-sustained in region 2, and

unstable in region 3 when considering enhanced vertical mixing. The blue star denotes the standard geometry and eigenmode using the parameters listed in Table 1. The values of the other parameters are the same as those listed in Table 1. Gray regions represent the ratios of e-folding time to period larger than 0.1. (c) and (d) are the same as (a) and (b), except that the ordinates represent the volume fraction of the subpolar ocean in the Southern Hemisphere $(V_3 + V_6)/V$.

Let us focus on the self-sustained modes in region 2. In the 6S model, the multicentennial timescale varies from 200 to 400 years in this phase space (Figs. 4b, d), with the volume increase of the upper ocean $(V_1 + V_2 + V_3)$, subpolar North Atlantic $(V_1 + V_4)$. These volumes significantly affect the oscillation period of the AMOC. Physically, changing $(V_1 + V_4)$ alters the area of deep-water formation, while changing $(V_1 + V_2 + V_3)$ modifies the influencing region of the upper branch of the AMOC, both of which are critical to the mass balance of the AMOC, and thus to a certain degree determine the turnover time of water in the Atlantic basin. In contrast, the volume of the subpolar South Atlantic $(V_3 + V_6)$ has much smaller effect on the period of the multicentennial oscillation (Fig. 4d), due to its less effect on the AMOC's mass balance.

The stability of the self-sustained oscillations is also quite sensitive to the volume changes of the upper ocean and subpolar North Atlantic (Figs. 4a, c). With the increasing volume of the upper ocean $(V_1 + V_2 + V_3)$, the e-folding time of the eigenmode decreases significantly (from 1600 to 400 years), suggesting that the oscillation modes can be converted from a weak unstable mode to a strong unstable mode in the absence of enhance vertical mixing (Figs. 4a, c). On the contrary, with the increasing volume of the subpolar North Atlantic $(V_1 + V_4)$, the e-folding time of the eigenmode increases significantly from 400 to 1600 years, suggesting a trend of being a stabilizing oscillation. However, the e-folding time of the eigenmode is less sensitive to the volume of the subpolar South Atlantic $(V_3 + V_6)$ (Fig. 4c), suggesting that the South Atlantic has a weak effect on the multicentennial oscillation. This result is qualitatively consistent our conclusion drawn in section 3a that the Southern Ocean has a minor impact on the multicentennial oscillation. This finding also agrees with the results of the one-hemisphere box model in LY22, in which only the role of subpolar North Atlantic is highlighted in the multicentennial oscillation.

4. Two-hemisphere box model with wind-driven circulation

To consider effect of wind-driven circulation, particularly the shallow meridional overturing circulation in the tropics, we need temperature equations, since the strength of such wind-driven circulation is roughly determined by the meridional temperature gradient. In fact, the meridional overturning circulation should include both thermohaline and wind-driven components, although in the Atlantic, the thermohaline component is much more important than the wind-driven component.

The wind-driven shallow meridional overturing circulation in the tropics, or the vertical component of the subtropical cells have an antisymmetric structure with respect to the equator (McCreary and Lu 1994; Schott et al. 2004). Including the temperature equations in the box model (termed as the 6TS model), the shallow wind-driven meridional overturning circulation can be thus parameterized (Fig. 1b). Equations of the 6TS model are written as follows,

$$V_1\dot{T}_1 = q(T_2 - T_1) + V_1\gamma(T_1^* - T_1) + q_n(T_2 - T_1) \tag{7a}$$

$$V_2\dot{T}_2 = q(T_3 - T_2) + V_2\gamma(T_2^* - T_2) - q_n(T_2 - T_1) - q_s(T_2 - T_3) \tag{7b}$$

$$V_3\dot{T}_3 = q(T_6 - T_3) + V_3\gamma(T_3^* - T_3) + q_s(T_2 - T_3) \tag{7c}$$

$$V_4\dot{T}_4 = q(T_1 - T_4) \tag{7d}$$

$$V_5\dot{T}_5 = q(T_4 - T_5) \tag{7e}$$

$$V_6\dot{T}_6 = q(T_5 - T_6) \tag{7f}$$

$$V_1\dot{S}_1 = q(S_2 - S_1) + F_{w1} + q_n(S_2 - S_1) \tag{7g}$$

$$V_2\dot{S}_2 = q(S_3 - S_2) + F_{w2} - q_n(S_2 - S_1) - q_s(S_2 - S_3) \tag{7h}$$

$$V_3\dot{S}_3 = q(S_6 - S_3) + F_{w3} + q_s(S_2 - S_3) \tag{7i}$$

$$V_4\dot{S}_4 = q(S_1 - S_4) \tag{7j}$$

$$V_5\dot{S}_5 = q(S_4 - S_5) \tag{7k}$$

$$V_6\dot{S}_6 = q(S_5 - S_6) \tag{7l}$$

A restoring boundary condition for surface temperature is employed in (7a-c), with γ being the restoring coefficient and set to 3.171×10^{-8} s^{-1} (corresponding to a 1-year restoring timescale). T_1^*, T_2^*, and T_3^* are the restoring temperatures for boxes 1, 2, and 3, respectively. q refers to the mass transport by the thermohaline circulation. q_n and q_s (units: Sv) refer to the mass transports by the northern and southern branches of the wind-driven circulation, respectively. For the convenience of discussion, we use 6TS_THC+WDC for the 6TS model considering both the thermohaline and wind-driven circulations; similarly, we use 6TS_THC (6TS_WDC) to represent the model considering only the thermohaline (wind-driven) circulation.

The equilibrium states of the 6TS model can be written as follows,

$$\overline{q}(\overline{T}_2 - \overline{T}_1) + V_1\gamma(T_1^* - \overline{T}_1) + \overline{q_n}(\overline{T}_2 - \overline{T}_1) = 0 \tag{8a}$$

$$\bar{q}(\bar{T}_3-\bar{T}_2)+V_2\gamma(T_2^*-\bar{T}_2)-\overline{q_n}(\bar{T}_2-\bar{T}_1)-\overline{q_s}(\bar{T}_2-\bar{T}_3)=0 \quad (8b)$$

$$\bar{q}(\bar{T}_6-\bar{T}_3)+V_3\gamma(T_3^*-\bar{T}_3)+\overline{q_s}(\bar{T}_2-\bar{T}_3)=0 \quad (8c)$$

$$\bar{T}_1=\bar{T}_4=\bar{T}_5=\bar{T}_6 \quad (8d)$$

$$\bar{q}(\bar{S}_1-\bar{S}_2)+\overline{q_n}(\bar{S}_1-\bar{S}_2)=F_{w1} \quad (8e)$$

$$\bar{q}(\bar{S}_2-\bar{S}_3)+\overline{q_n}(\bar{S}_2-\bar{S}_1)+\overline{q_s}(\bar{S}_2-\bar{S}_3)=F_{w2} \quad (8f)$$

$$\bar{q}(\bar{S}_3-\bar{S}_6)+\overline{q_s}(\bar{S}_3-\bar{S}_2)=F_{w3} \quad (8g)$$

$$\bar{S}_1=\bar{S}_4=\bar{S}_5=\bar{S}_6 \quad (8h)$$

$$F_{w1}+F_{w2}+F_{w3}=0 \quad (8i)$$

Here, different boundary conditions are used for cases with and without the wind-driven circulation (Table 1). For the 6TS_THC model without the wind-driven circulation, $\overline{q_n}=\overline{q_s}=0$, T_1^*, T_2^*, and T_3^* are set to 3.7, 24.5, and 7.7 °C, respectively. For the 6TS_THC+WDC model, $\overline{q_n}$ and $\overline{q_s}$ are not zero, F_{w1}, F_{w2}, and F_{w3} are set to -8.97×10^7, 10.79×10^7, and -1.82×10^7 psu m^3 s^{-1}, and T_1^*, T_2^*, and T_3^* are set to 3.4, 24.6, and 7.6 °C, respectively, to keep the equilibrium salinities and temperatures identical to those in the 6TS_THC model. In this paper, we assume $\bar{q}$ and $\overline{q_n}$ ($\overline{q_s}$) are positive, representing the clockwise climatological thermohaline circulation in the Atlantic, and mean northward (southward) transport in the Northern (Southern) Hemisphere, respectively. $\overline{q_n}$ ($\overline{q_s}$) always transports heat poleward because the upper-ocean water moving poleward is always warmer than the lower-ocean water moving equatorward.

The linearized equations of the 6TS model are given below,

$$V_1\dot{T}_1'=\bar{q}(T_2'-T_1')+q'(\bar{T}_2-\bar{T}_1)-V_1\gamma T_1'+\overline{q_n}(T_2'-T_1')+q_n'(\bar{T}_2-\bar{T}_1) \quad (9a)$$

$$V_2\dot{T}_2'=\bar{q}(T_3'-T_2')+q'(\bar{T}_3-\bar{T}_2)-V_2\gamma T_2'-\overline{q_n}(T_2'-T_1')-q_n'(\bar{T}_2-\bar{T}_1)-\overline{q_s}(T_2'-T_3')-q_s'(\bar{T}_2-\bar{T}_3) \quad (9b)$$

$$V_3\dot{T}_3'=\bar{q}(T_6'-T_3')+q'(\bar{T}_6-\bar{T}_3)-V_3\gamma T_3'+\overline{q_s}(T_2'-T_3')+q_s'(\bar{T}_2-\bar{T}_3) \quad (9c)$$

$$V_4\dot{T}_4'=\bar{q}(T_1'-T_4') \quad (9d)$$

$$V_5\dot{T}_5'=\bar{q}(T_4'-T_5') \quad (9e)$$

$$V_6\dot{T}_6'=\bar{q}(T_5'-T_6') \quad (9f)$$

$$V_1\dot{S}_1'=\bar{q}(S_2'-S_1')+q'(\bar{S}_2-\bar{S}_1)+\overline{q_n}(S_2'-S_1')+q_n'(\bar{S}_2-\bar{S}_1) \quad (9g)$$

$$V_2\dot{S}_2'=\bar{q}(S_3'-S_2')+q'(\bar{S}_3-\bar{S}_2)-\overline{q_n}(S_2'-S_1')-q_n'(\bar{S}_2-\bar{S}_1)-\overline{q_s}(S_2'-S_3')-q_s'(\bar{S}_2-\bar{S}_3) \quad (9h)$$

$$V_3\dot{S}_3'=\bar{q}(S_6'-S_3')+q'(\bar{S}_6-\bar{S}_3)+\overline{q_s}(S_2'-S_3')+q_s'(\bar{S}_2-\bar{S}_3) \quad (9i)$$

$$V_4\dot{S}_4'=\bar{q}(S_1'-S_4') \quad (9j)$$

$$V_5\dot{S}_5'=\bar{q}(S_4'-S_5') \quad (9k)$$

$$V_6\dot{S}_6' = \bar{q}(S_5' - S_6') \tag{9l}$$

where q' is determined by both temperature and salinity anomalies,

$$q' = q_T' + q_S' = \lambda(\Delta\rho_T' + \Delta\rho_S') \tag{10a}$$

$$\Delta\rho_T' = -\rho_0\alpha[\delta(T_1' - T_3') + (1-\delta)(T_4' - T_6')] \tag{10b}$$

$$\Delta\rho_S' = \rho_0\beta[\delta(S_1' - S_3') + (1-\delta)(S_4' - S_6')] \tag{10c}$$

Here, the wind-driven volume transports in the tropics can be roughly scaled as the Ekman transport, which is proportional to the zonal surface wind stress, that is, $V_E = -\frac{\tau^x}{\rho_0 f}$, where τ^x is the zonal surface wind stress, and f is the Coriolis parameter. According to Vallis (2017), the ocean surface wind stress can be parameterized by surface wind speed and finally scaled as to be proportional to the meridional gradient of the surface air temperature or sea surface temperature (SST) based on thermal wind equation, that is,

$$\tau^x \approx \frac{\rho_a g h C_D |u|}{T_0 f}\frac{\partial T}{\partial y} \sim \alpha\frac{\partial SST}{\partial y} \tag{11}$$

where u is ocean surface zonal wind speed, ρ_a is the air density, C_D is the drag coefficient, h is depth of atmospheric boundary and T_0 is the mean surface air temperature in the tropics. Therefore,

$$V_E = -\frac{\tau^x}{\rho_0 f} \sim -\frac{\alpha}{\rho_0 f}\frac{\partial SST}{\partial y} \sim (T_2 - T_1) \tag{12}$$

Physically, we can simply understand Eq. (12) as follows: high (low) temperature in the tropics (extratropics) drives a normal clockwise Hadley Cell, and therefore generates easterlies in the surface tropics due to the Coriolis effect on the lower southward branch of the Hadley Cell, which in turn drives a northward Ekman flow. A stronger poleward SST contrast will result in a stronger northward Ekman transport, which, in turn, would reduce the poleward SST gradient. This is negative feedback between the SST gradient and the wind-driven circulation.

Finally, the wind-driven volume transports q_n and q_s can be parameterized as follows,

$$q_n = \overline{q_n} + q_n' = \kappa_n(\bar{T}_2 - \bar{T}_1) + \kappa_n(T_2' - T_1') \tag{13a}$$

$$q_s = \overline{q_s} + q_s' = \kappa_s(\bar{T}_2 - \bar{T}_3) + \kappa_s(T_2' - T_3') \tag{13b}$$

where κ_n and κ_s are parameters related to thermal wind and wind-driven gyre mechanisms and are set to the same value of about 0.30 Sv °C^{-1}, which is chosen to make $\overline{q_n}$ and $\overline{q_s}$ as 5.9 Sv and 5.1 Sv, respectively, corresponding to northward and southward heat transports of about 0.46 PW and 0.34 PW, respectively, and equilibrium northward and southward salinity transport of about 17.7 and 15.8

Sv psu. We would like to emphasize that these equilibrium values were deliberately chosen to align with those produced in many complex models (Treguier et al. 2014; Vallis and Farneti 2009).

a. Effects of wind-driven circulation

Figure 5 shows dependences of damping rate [Re(ω)] and frequency [Im(ω)] on λ, using the parameters listed in Table 1. Re(ω) in the 6TS_THC model is smaller than that in the 6S model (Figs. 5a, c), suggesting that thermal processes play a dampening role in the AMOC multicentennial oscillation. Detailed discussion about the impact of the thermal processes on the thermohaline circulation can be found in our publication of YYL24. With the wind-driven circulation, Re(ω) becomes even smaller and the multicentennial mode becomes more damped under the same λ (Figs. 5a, c). When λ = 21.3 Sv kg^{-1} m^3, the e-folding times of the multicentennial mode in the 6S, 6TS_THC, and 6TS_THC+WDC models are about 930, –2800, and –320 years, corresponding a weakly unstable mode, a weakly damped mode, and a strongly damped mode, respectively. These results also suggest that the wind-driven circulation has a strong damping effect in addition to the thermal processes. However, the maximum Im(ω) does not change too much with the added processes (Fig. 5b), which corresponds to the shortest period of about 340±20 years.

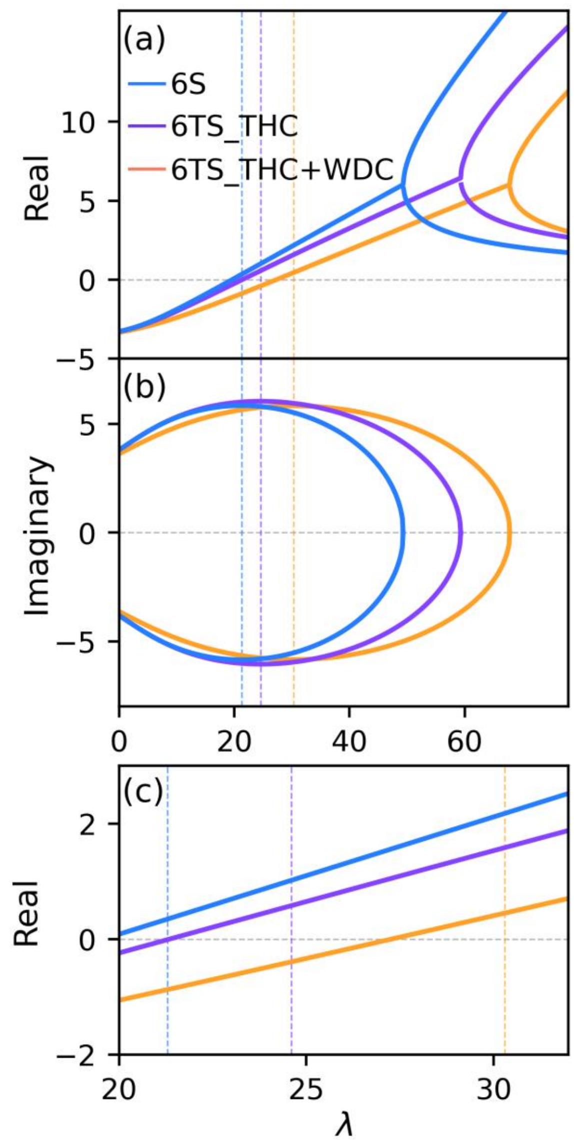

FIG. 5. Dependences of (a) damping rate [Re(ω)] and (b) frequency [Im(ω)] of multicentennial modes on λ in the 6S, 6TS_THC, and 6TS_THC+WDC models. Solid curves are for $\lambda > 0$; dashed curves are for $\lambda \leq 0$ and have no physical meaning. The vertical dashed blue, purple, and orange lines are for $\lambda = 21.3$, $\lambda = 24.6$, and $\lambda = 31.3$ Sv kg^{-1} m^3, denoting the position when the frequency of the multicentennial mode reaches the maximum in the three models, respectively. The units of the ordinate are 10^{-10} s^{-1}. Parameters used here are listed in Table 1. (c) Same as (a), but the abscissa axis is zoomed-in. Colored lines are noted in panel (a).

The eigenmodes in the 6TS model under $\lambda = 21.3$ Sv kg^{-1} m^3 are too damped to become a self-sustained oscillation. Given the higher sensitivity of the thermohaline circulation to the density change, for example, $\lambda = 24.6$ Sv kg^{-1} m^3, the multicentennial mode in the 6TS_THC model has a period of about 330 years and an e-folding time of 550 years. Set $\lambda = 31.3$ Sv kg^{-1} m^3 in the 6TS_THC+WDC model, the multicentennial mode has a period of 340 years and an e-folding time of

740 years (Table 2). Such an alternative of λ value corresponds to the maximum $\mathrm{Im}(\omega)$ (the shortest period) and produces the weakly unstable eigenmode (Fig. 5), which can be easily converted to a self-sustained oscillation when enhanced vertical mixing is added in the subpolar North Atlantic.

Adding enhanced vertical mixing in the subpolar North Atlantic boxes in the 6TS model [Eq. (9)], the equations become,

$$V_1\dot{T}_1' = \cdots - k_m(T_1' - T_4') \tag{14a}$$

$$V_4\dot{T}_4' = \cdots + k_m(T_1' - T_4') \tag{14b}$$

$$V_1\dot{S}_1' = \cdots - k_m(S_1' - S_4') \tag{14c}$$

$$V_4\dot{S}_4' = \cdots + k_m(S_1' - S_4') \tag{14d}$$

Here, λ is set to 24.6 and 31.3 Sv kg^{-1} m^3 for the 6TS_THC and 6TS_THC+WDC models, respectively. The results are obtained from numerical integrations of these models. The self-sustained multicentennial oscillation is manifested in all variables, such as S_1', T_1', and q' (Fig. 6). The presence of the wind-driven circulation weakens the amplitude of the oscillation remarkably (Figs. 6a-c), with the amplitude of q' weakened by about 30% (from 0.35 to 0.23 Sv) (Fig. 6c), while it only lengthens the oscillation period slightly, with the period changing from ~330 to 340 years (Fig. 6f).

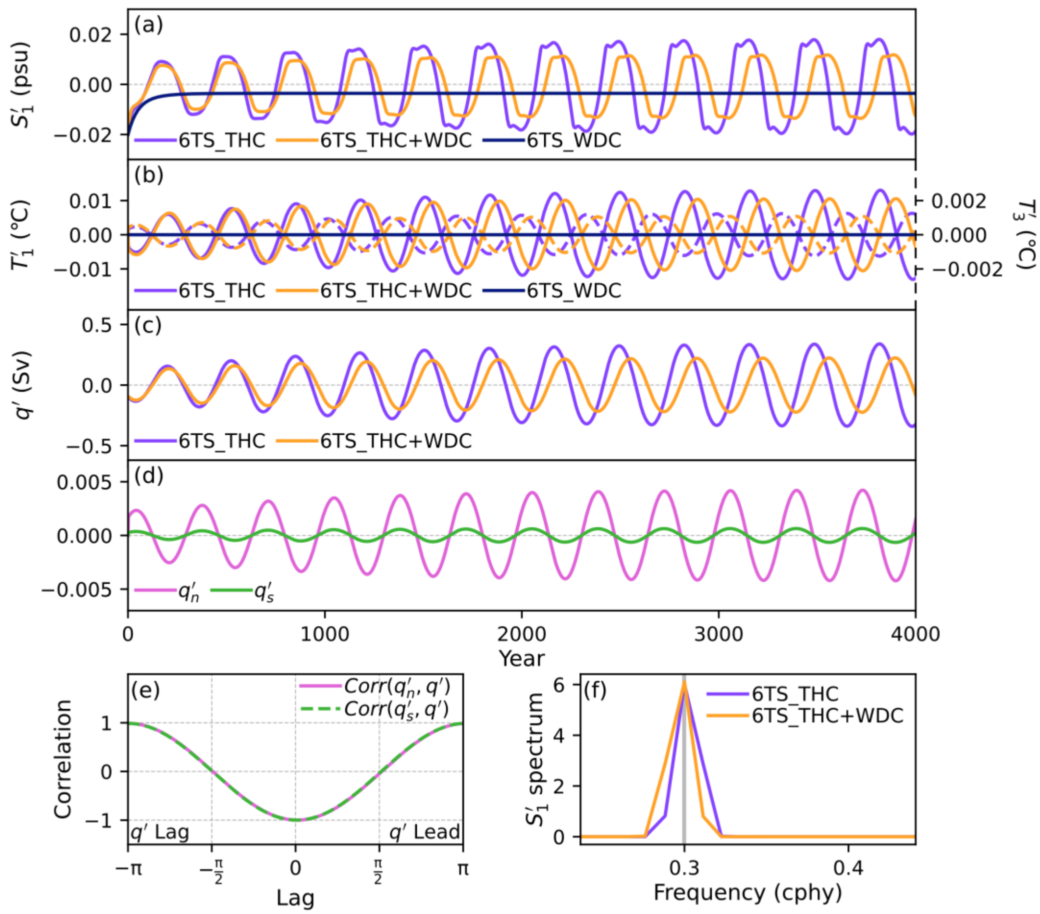

FIG. 6. Time series of (a) S_1' (units: psu) and (b) T_1' and T_3' (units: °C) in the 6TS_THC, 6TS_THC+WDC, and 6TS_WDC models. In (b), solid (dashed) curves are for T_1' (T_3'). (c) Time series of q' (units: Sv) in these models. (d) Time series of northward q_n' and southward q_s'. (e) Lead-lag correlation coefficients of q' with q_n' and q_s'. For negative lags, q_n' and q_s' lead. (f) Power spectra of S_1' in 6TS_THC and 6TS_THC+WDC; the abscissa is cycle per a hundred year (cphy). The values of λ in the three cases are given in the title of Table 2. Other parameters use the values in Table 1.

The mechanism of the wind-driven circulation affecting the multicentennial mode in the 6TS_THC+WDC model can be explained as follows. There is a compensation effect between the shallow wind-driven meridional overturning circulation and the thermohaline circulation. As shown in Fig. 6e, q_n' and q_s' are inversely related to q'; q_n' is much larger and more important than q_s' (Fig. 6d). There are two negative feedbacks between q' and q_n' in the North Atlantic. Starting with a positive perturbation of q', the perturbation advection $q'(\overline{T}_2 - \overline{T}_1)$ transports more warm water northward, reducing the meridional temperature difference and leading to an increase of T_1' and to decreases of $T_2' - T_1'$ and q_n'. Hence, with increasing q', the weakened q_n' transports less tropical saline water northward by decreasing the perturbation advection of mean salinity $[q_n'(\overline{S}_2 - \overline{S}_1)]$, resulting in declines of S_1' and q' (Fig. 7c). Another negative feedback is related to the mean advection $[\overline{q_n}(S_2' - S_1')]$ via the wind-driven circulation, playing a similar role with the mean advection $[\bar{q}(S_2' - S_1')]$ via the thermohaline circulation. Increasing q' leads to increasing S_1' through perturbation advection $[q'(\overline{S_2} - \overline{S_1})]$ via the thermohaline circulation, which results in a decline of the mean advection $[\overline{q_n}(S_2' - S_1')]$ by the wind-driven circulation and, in turn, restrains S_1' and q' (Fig. 7c).

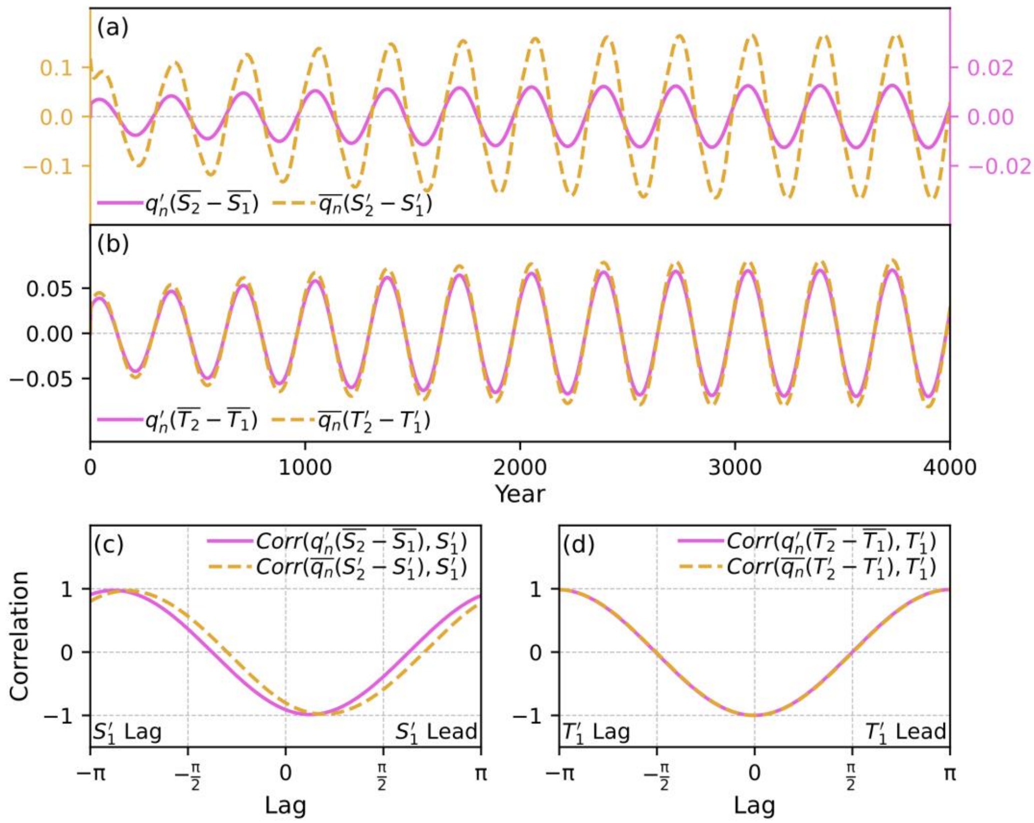

FIG. 7. (a) Time series of salinity terms by the wind-driven circulation (units: Sv psu) in Eq. (9g), which are $q_n'(\overline{S_2} - \overline{S_1})$ and $\overline{q_n}(S_2' - S_1')$ in the 6TS_THC+WDC model. (b) Time series of temperature terms (units: Sv °C) by the wind-driven circulation in Eq. (9a), which are $q_n'(\overline{T_2} - \overline{T_1})$ and $\overline{q_n}(T_2' - T_1')$ in the 6TS_THC+WDC model. (c) Lead-lag correlation coefficients of S_1' with $q_n'(\overline{S_2} - \overline{S_1})$ and $\overline{q_n}(S_2' - S_1')$. (d) Lead-lag correlation coefficients of T_1' with $q_n'(\overline{T_2} - \overline{T_1})$ and $\overline{q_n}(T_2' - T_1')$. For negative lags, salinity and temperature terms lead. λ is set to 31.3 Sv kg^{-1} m^3, and other parameters use the values in Table 1.

Contrary to the salinity processes, the wind-driven thermal processes affect the multicentennial mode through two positive feedbacks (Fig. 7d). The first one is the positive feedback caused by mean wind-driven advection $[\overline{q_n}(T_2' - T_1')]$. With the positive perturbation of q', the growth of T_1' reduces the mean wind-driven advection $[\overline{q_n}(T_2' - T_1')]$, which in turn reduces T_1' and helps promote q'. The second one is the positive feedback of perturbation wind-driven advection $[q_n'(\overline{T_2} - \overline{T_1})]$. With the positive perturbation of q' thereby negative perturbation of q_n', the perturbation advection $[q_n'(\overline{T}_2 - \overline{T}_1)]$ transports less equatorial warm water northward, restraining the rise of T_1' (Fig. 7d) and promoting q'.

Southward wind-driven advection plays a less prominent role in affecting the multicentennial oscillation due to the smaller variability of S_3' and T_3' (Figs. 3a, 6b). The compensation effect between the wind-driven and thermohaline circulations is also valid in the Southern Hemisphere (Fig. 6e). As an increased q' transports more cold water from the subpolar South Atlantic to the tropics through perturbation thermohaline advection, T_2' decreases, resulting in declines of $T_2' - T_3'$ and q_s'. Then, the weakened q_s' transports less warm and saline water from the tropics into the subpolar South Atlantic by decreasing the perturbation advection, $q_s'(\overline{S}_2 - \overline{S}_3)$ and $q_s'(\overline{T}_2 - \overline{T}_3)$. As a result, both S_3' and T_3' decrease (Figs. 8c, d), which tend to help and restrain the growth of q', respectively. The other feedback is related to the mean wind-driven advection, $\overline{q}_s(S_2' - S_3')$ and $\overline{q}_s(T_2' - T_3')$, playing opposite roles against the mean advection feedback of the thermohaline circulation and decreasing both S_3' and T_3'. In short, the southward wind-driven transport affects the multicentennial oscillation through the positive feedback induced by salinity processes and negative feedback induced by thermal processes; however, these feedbacks (Figs. 8a, b) are much weaker than those in the North Atlantic (Figs. 7a, b).

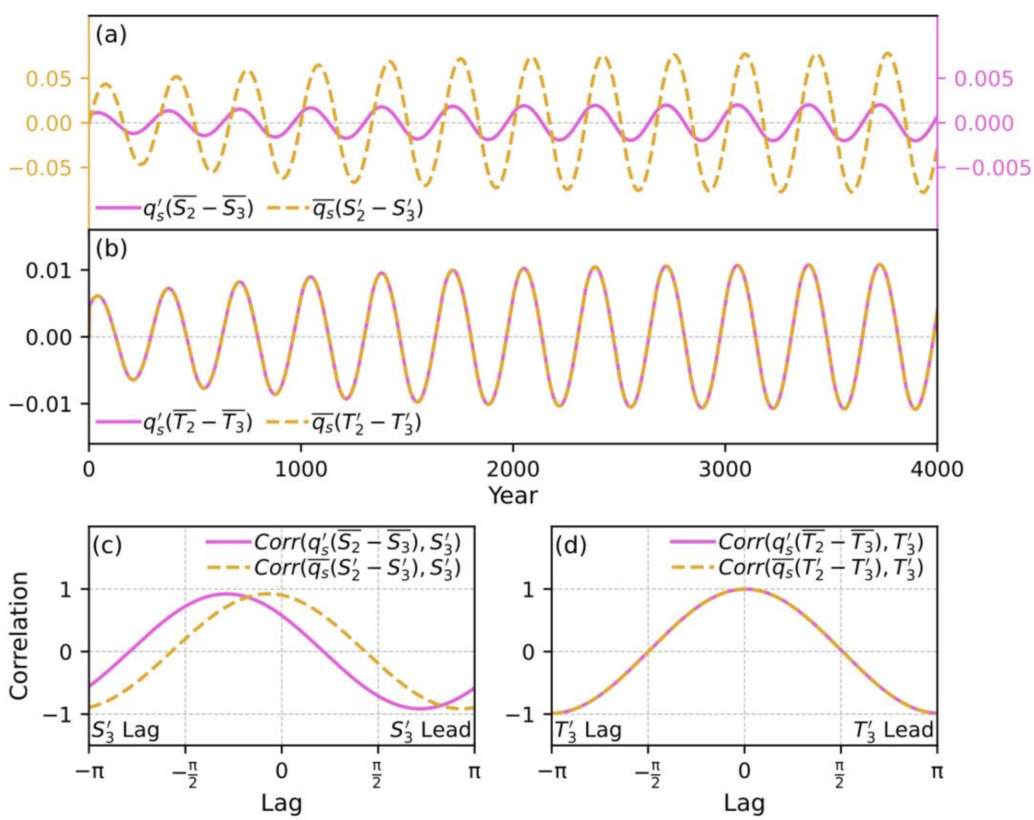

FIG. 8. Same as Fig. 7, but for the wind-driven circulation in the tropical ocean of Southern Hemisphere.

b. Stability analysis in the presence of wind-driven circulation only

To demonstrate its essential role in the multicentennial oscillation, we shut the thermohaline circulation down (i.e., $\bar{q}$ = 0 and λ = 0), so there is only the wind-driven circulation in the box model. Temperature and salinity anomalies show no oscillation once the thermohaline circulation is shut down (dark blue curves in Figs. 6a, b). Now the system has only heat and salinity transports in the upper ocean by the wind-driven circulation, in which the variability is controlled only by the temperature variability in the upper ocean. Eqs. (9a-c) can be rewritten as follows,

$$V_1\dot{T}_1' = -V_1\gamma T_1' + \overline{q_n}(T_2' - T_1') + q_n'(\bar{T}_2 - \bar{T}_1) \tag{15a}$$

$$V_2\dot{T}_2' = -V_2\gamma T_2' - \overline{q_n}(T_2' - T_1') - q_n'(\bar{T}_2 - \bar{T}_1) - \bar{q}_s(T_2' - T_3') - q_s'(\bar{T}_2 - \bar{T}_3) \tag{15b}$$

$$V_3\dot{T}_3' = -V_3\gamma {T_3}' + \bar{q}_s(T_2' - T_3') + q_s'(\bar{T}_2 - \bar{T}_3) \tag{15c}$$

Subtracting Eq. (15a) and Eq. (15c) from Eq. (15b), respectively, we have,

$$\dot{T}_n' = (\sigma_1(\overline{q_n} + \kappa_n\overline{T_n}) - \gamma)T_n' + \sigma_2(\bar{q}_s + \kappa_s\bar{T}_s)T_s' \tag{16a}$$

$$\dot{T}_s' = \sigma_2(\overline{q_n} + \kappa_n\overline{T_n})T_n' + (\sigma_3(\bar{q}_s + \kappa_s\bar{T}_s) - \gamma)T_s' \tag{16b}$$

where $\overline{T_n} = \bar{T}_2 - \bar{T}_1$, $\bar{T}_s = \bar{T}_2 - \bar{T}_3$, $\sigma_1 = \frac{1}{V_1} - \frac{1}{V_2}$, $\sigma_2 = -\frac{1}{V_2}$, and $\sigma_3 = \frac{1}{V_3} - \frac{1}{V_2}$.

With $\overline{q_n} = \kappa_n\overline{T_n}$ and $\bar{q}_s = \kappa_s\bar{T}_s$, we can further define the following quantities:

$$C_1 = \sigma_1(\overline{q_n} + \kappa_n\overline{T_n}) - \gamma = 2\sigma_1\overline{q_n} - \gamma$$

$$C_2 = \sigma_2(\bar{q}_s + \kappa_s\bar{T}_s) = 2\sigma_2\bar{q}_s$$

$$C_3 = \sigma_2(\overline{q_n} + \kappa_n\overline{T_n}) = 2\sigma_2\overline{q_n}$$

$$C_4 = \sigma_3(\bar{q}_s + \kappa_s\bar{T}_s) - \gamma = 2\sigma_3\bar{q}_s - \gamma$$

Assuming the solution has the form of $T_n' = Ae^{\omega t}$, Eq. (16) has eigenvalues,

$$\omega = \frac{1}{2}\left[(C_1 + C_4) \pm \sqrt{(C_1 + C_4)^2 - 4(C_1C_4 - C_2C_3)}\right] \tag{17}$$

The eigenvalues lie on the value Δ that is defined by,

$$\Delta = (C_1 + C_4)^2 - 4(C_1C_4 - C_2C_3) = [4(\sigma_1\overline{q_n} - \sigma_3\bar{q}_s)^2 + 16{\sigma_2}^2\overline{q_n}\bar{q}_s] > 0 \tag{18}$$

Here, Δ is always positive; and there will be no oscillatory solutions in this system, as long as the wind-driven circulation transports heat and salinity poleward (i.e., $\overline{q_n}$ > 0 and $\bar{q}_s$ > 0). In fact, Eq. (15) clearly shows that the tendencies of T_1', T_2', and T_3' are always damped by T_1', T_2', and T_3' themselves.

As the temperature anomaly increases, its tendency will be in turn killed. The theoretical solution in the presence of only wind-driven circulation agrees well with the numerical results in section 4a. From another perspective, the inclusion of the northward $\overline{q_n}$ (southward $\overline{q_s}$) offers two negative (positive) salinity feedbacks and two positive (negative) temperature feedbacks, which are unable to produce oscillations. In other words, only the presence of the thermohaline circulation can produce both negative and positive feedbacks for the thermal and saline processes simultaneously, which serves as a sufficient and necessary condition for the multicentennial oscillation.

5. Linear oscillations excited by stochastic forcing

In this section, we further investigate the multicentennial oscillation under stochastic forcing, following the approach in LY22. With the inclusion of the stochastic freshwater and heat inputs in the subpolar North Atlantic, Eq. (3a) is rewritten as follows,

$$V_1 \dot{S}_1' = \cdots + V_1 N \tag{19a}$$

$$V_1 \dot{T}_1' = \cdots + V_1 N \tag{19b}$$

where N represents the external stochastic forcing, which is a red noise generated from the model of Auto-Regressive-1 and has an autocorrelated e-folding decay time of 10 years. λ is set to 21.0 and 23.0 Sv kg^{-1} m^3 for the 6TS_THC and 6TS_THC+WDC models, respectively, indicating that the internal oscillations are damped oscillations due to the negative real part of the eigenmodes (Fig. 5a). Other parameters are the same as those in Table 1.

Stochastic forcing can turn such damped oscillatory mode into a sustained oscillation even without enhanced vertical mixing (Figs. 9a-c). The ratio of the S_1' spectrum (Fig. 9f) to the spectrum of the noise (Fig. 9e), i.e., signal-to-noise ratio (SNR), is shown in Fig. 9g, in which the SNR reaches a maximum at the period of about 320 years. This principal period is identical to the period obtained from the linear stability analysis in section 2, proving that the multicentennial mode is an intrinsic mode of the Atlantic Ocean. Furthermore, it is clear that the wind-driven circulation plays a damping role in the oscillation (Figs. 9a-c) and lengthens its period slightly (Fig. 9g). After adding the wind-driven circulation, the SNR has a lower power with the peak value corresponding to 340 years (orange curve in Fig. 9g). Once the thermohaline circulation is shut down, the SNR has no peak (blue curve in Fig. 9g), suggesting no preferred period in the system.

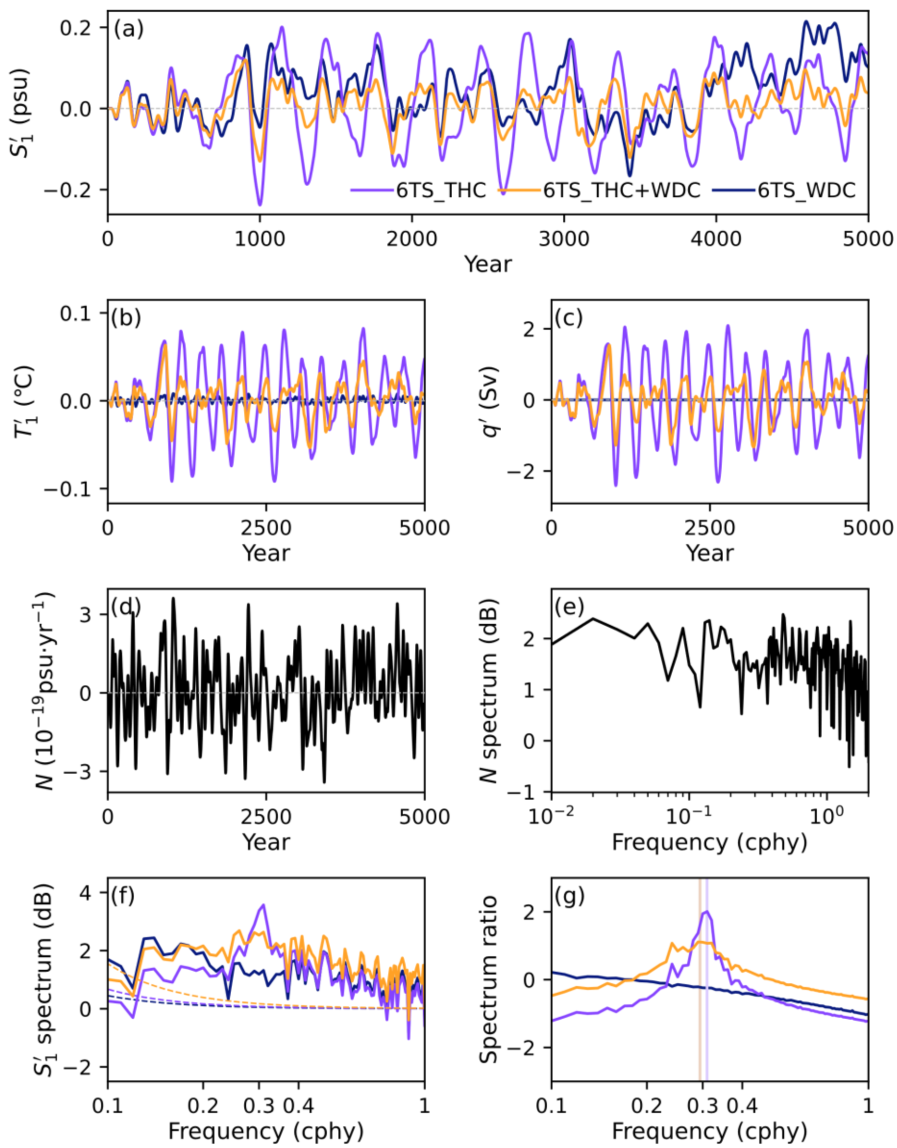

FIG. 9. Time series of (a) S_1', (b) T_1', and (c) q' in the 6TS_THC model, the 6TS_THC+WDC model, and the 6TS_WDC model, forced by stochastic freshwater and heat flux. λ is set to 21.0 and 23.0 Sv kg^{-1} m^3 for the 6TS_THC and 6TS_THC+WDC modes, respectively; and damped oscillatory modes are obtained in the presence of the thermohaline circulation. Other parameters take the values in Table 1. (d) Time series of stochastic freshwater and heat flux (units: 10^{-19} psu yr^{-1} and 10^{-19} °C yr^{-1}), which are red noises with identical magnitude but different units; and (e) their power spectra (units: dB). (f) The power spectra of S_1' for three cases with the confidence level 95%. (g) The ratios of S_1' spectrum to the noise spectrum (units: dB), with peaks around 0.31 and 0.29 cycles per a hundred year (cphy) (320 and 340 years) for the 6TS_THC and 6TS_THC+WDC modes, respectively. Colored curves are noted in panel (a).

6. Summary and discussion

In this study, we investigate the multicentennial oscillation of the AMOC in a two-hemisphere box model, which is an advancement from one-hemispheric theoretical model. In the two-hemisphere model, the AMOC anomaly is parameterized to be linearly proportional to the density difference between the northern and southern subpolar boxes. A weakly unstable multicentennial oscillation mode with a period of about 340 years is identified in the two-hemisphere box model under the parameters in Table 1. This result aligns with the findings of LY22, indicating comparable periods in the one-hemisphere and two-hemisphere models, because both the total ocean basin volume and mean AMOC strength in this study are approximately twice of those in LY22. Similar to LY22 and YYL24, the sustained multicentennial oscillation can be realized by enhanced vertical mixing in the subpolar North Atlantic or external stochastic forcing. We emphasize that the multicentennial mode is an intrinsic mode of the thermohaline circulation.

The wind-driven circulation, particularly the shallow meridional overturning circulation in the tropics, or the vertical component of the subtropical cells, plays a dampening effect on the multicentennial oscillation. The primary effect of the wind-driven circulation is to weaken the amplitude of the multicentennial oscillation, as its effect on the multicentennial oscillation period can be neglected. The stabilized effect of the wind-driven circulation occurs because of the negative feedback between the thermohaline and wind-driven circulations through the salinity processes in the North Atlantic. The compensation between the strengths of thermohaline and wind-driven circulations occurs because a stronger thermohaline circulation causes a stronger meridional heat transport, which, in turn, reduces the meridional temperature gradient, weakening the wind-driven circulation. This further leads to less poleward salinity transport and slows down the growth of salinity anomaly in the subpolar North Atlantic, resulting in the weakening of the multicentennial oscillation. Note that the wind-driven circulation alone cannot cause oscillatory behavior in such a two-hemisphere box model. Once the thermohaline circulation is shut down, the multicentennial oscillation ceases to exist, suggesting that the thermohaline circulation is a necessary condition in generating the multicentennial oscillation. The 6TS model including the wind-driven circulation is more realistic, since the oceanic thermal processes and the Southern Ocean are included simultaneously.

To better understand eigenmodes in the two-hemisphere box model, a further simplified version of the 6S model, referred to as the 3-box model (the 3S model; Appendix B, Fig. B1), is constructed. Despite its simplicity, the 3S model gives a nearly identical oscillatory eigenmode to that of the 6S model (Fig. B1), and to that reported in Scott et al. (1999) as well, under similar parameters. This suggests that the simplification of the box structure and basin geometry in the 3S model does not change the fundamentals of the multicentennial eigenmode found in the 6S model; thus, the theoretical solution of the 3S model can offer a deeper understanding of the multicentennial mode. For example, as detailed in Appendix B, the theoretical solution to the period of the multicentennial oscillation in the 3S model can be written as,

$$T \sim \frac{2\pi}{\bar{q}}\left(\frac{V_1 V_2}{\frac{V_2}{V_1}M^2-\left(\frac{V_2}{V_1}-\frac{V_2}{V_3}+1\right)M+1}\right)^{\frac{1}{2}}, \text{ where } M=\frac{V_3}{V_2}\left(\frac{V_2F_{w1}-V_1F_{w2}}{V_3F_{w1}-V_1F_{w3}}\right), \quad (20)$$

which indicates that the mean AMOC strength, the basin volume and geometry, and surface freshwater fluxes in different ocean basins can affect the oscillation period significantly.

In both the 6S and 3S models, we observe a roughly linear relationship between total basin volume and oscillatory period, and an inversely proportional relationship between the mean AMOC strength and the oscillatory period (Fig. 10). In larger ocean basins, such as the Pacific Ocean, the period of the multicentennial oscillation could be much longer (Fig. 10a), if the thermohaline circulation exists in the Pacific instead of in the Atlantic. This could have occurred in the Earth's history (Burls et al. 2017; Okazaki et al. 2010). Paleoclimatic evidence has suggested that the NADW formation began around 15 million years ago, before which the deep-water formation may have occurred in the North Pacific (Okazaki et al. 2010). It is then straightforward that the weaker the AMOC strength is, the longer period the multicentennial oscillation has (Fig. 10b). It is interesting to notice that there could have millennial oscillation in the global ocean with period of about 1500 years, if the mean AMOC is half of the value of the present climate (Fig. 10b). This might provide a clue to understand the Dansgaard-Oeschger events (or called the D-O cycle in some literature; Dansgaard et al. 1984) during the Last Glacial Maximum period or the Bond cycles (Bond et al. 1997) during the Holocene.

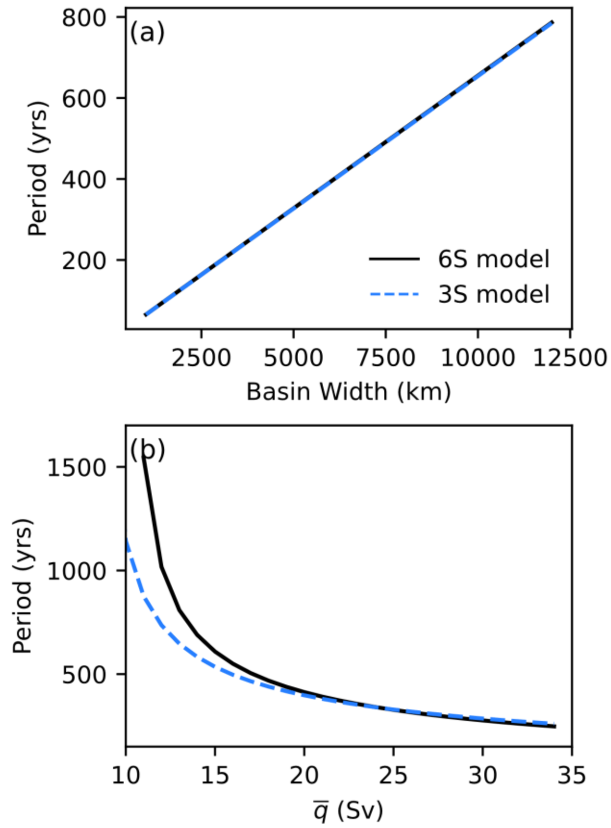

FIG. 10. Dependences of the minimum period of the multicentennial oscillatory mode on (a) mean basin width and (b) $\overline{q}$ in the 6S and 3S models, respectively. The black curve is the results from the numerical solutions of the 6S model. The dashed blue curve is the results from the theoretical solution of the 3S model.

In addition to the total basin volume, the basin geometry plays a significant role in determining the period of the multicentennial oscillation, as shown in Fig. 4 and Eq. (20). This basin geometry encompasses various factors, such as the depth of the upper and lower oceans, the division between the tropics and extratropics, the definition of the deep-water formation region, and so on. The basin geometry offers numerous possibilities; and it is not immediately evident that the multicentennial oscillation would have a specific period. However, under a “reasonably realistic” basin geometry, it is highly likely that the ocean would exhibit an oscillation with a centennial to millennial timescale, known as the multicentennial oscillation.

The period of the multicentennial oscillation is also closely related to climatological surface freshwater fluxes in different basins [Eq. (20)], consistent with the results of Sévellec et al. (2006). Sévellec et al. (2006) believed that the geometry of the forcing affects the period and growth rate of the multicentennial oscillation largely. The sensitivity of the multicentennial oscillation to surface freshwater flux is complex, and is not studied in this paper, because changes in the mean surface freshwater flux may lead to regime shift and multi-equilibrium states of the climate system. Therefore, surface freshwater flux is simply prescribed in this paper. The mean surface freshwater flux determines equilibrium salinity, which, in turn, determines the linear closure parameter λ (Appendix B, Eq. (B14)). Besides, Eq. (B8) reveals the significant interaction between surface freshwater flux and closure parameter λ. However, we also found that under certain conditions, the surface freshwater flux did not have a significant impact on the period. For example, when the equilibrium salinity of the subpolar South Atlantic is equal to that of the other regions (i.e., $\overline{S_2} = \overline{S_3}$ or $\overline{S_1} = \overline{S_3}$), the multicentennial oscillation period only depends on the basin geometry and the strength of the AMOC (Appendix B, Eqs. (B16) and (B17)). The derivation in Appendix B indicates a clear physical connection between the surface freshwater flux and multicentennial oscillation; further studies will be carried out in the future.

Although the multicentennial oscillation can be an intrinsic mode of the thermohaline circulation, its sustainability in the real world is a serious concern. The multicentennial oscillation of the AMOC is strongly influenced by changing climate background, such as variations in sea-surface freshwater flux, the deep-water formation region, the AMOC strength, etc. In unfavorable environmental conditions, the detection of the multicentennial oscillation in the real world might be challenging, which may explain the weak signals of the multicentennial oscillation retrieved from proxy data (Stocker and Mysak 1992).

Besides the possibility that the multicentennial oscillation might become the millennial timescale in the climate with a weak AMOC (Fig. 10b), there is a millennial mode in the two-hemisphere box model itself (red curves in Figs. 2a, b). Even though the physical meaning of this millennial mode is unclear, it might also provide a clue for understanding the D-O events and Bond cycles. Inspired by Sakai and Peltier (1995, 1996, 1997), which reported that increased surface freshwater fluxes could lengthen the period of the multicentennial oscillation to the millennial timescale, we plan to conduct a study aiming to excite the millennial oscillation, with a focus on the influence of surface freshwater flux from the Arctic sea-ice and Antarctic ice-sheet. We will develop an air-sea coupled box model, in which a varying surface freshwater flux can be introduced. We hope to not only deliberate the sensitivity of the multicentennial oscillation to surface freshwater fluxes, but also identify a less damped millennial mode. Such results may shed light on mechanisms of long-term climate evolution since the Last Glacial Maximum.

Acknowledgements.

This research is jointly supported by the NSF of China (Nos. 42230403, 42288101, 41725021, and 91737204) and by the foundation at the Shanghai Frontiers Science Centre of Atmosphere-Ocean Interaction of Fudan University.

Data Availability Statement.

This is a theory-based article; thus, no datasets are generated.

Conflict of interest

The authors have no relevant financial or non-financial interests to disclose.

APPENDIX A

Linear relation between AMOC and meridional density difference in the Atlantic

Studies have demonstrated a linear relation between the AMOC index and the density difference between the North Atlantic and South Atlantic, despite that the regions selected may be different (Griesel and Maqueda 2006; Hughes and Weaver 1994; Rahmstorf 1996; Thorpe et al. 2001; Wood et al. 2019). Here, we validate the parameterization of the AMOC index in the two-hemispheric box model utilizing results from two coupled climate models, namely the Community Earth System Model (CESM, version 1.0) developed by the National Centre for Atmospheric Research (NCAR) and EC-Earth3-Veg-LR. The AMOC index is defined as the maximum meridional streamfunction in the region of 20°-70°N between 200 and 3000 m in the Atlantic. The meridional density difference is defined by taking the difference in density anomalies integrated over a depth of 4000 m between a North Atlantic box and a South Atlantic box. The North Atlantic box covers the region of 40°-50°W, 43°-60°N; the South Atlantic 25°-50°W, 45°-55°S; and the subtropic box, 20°-65°W, 20°-35°N (Fig. A1a). These definitions are applied in the same way for both coupled models.

A long simulation using the CESM1.0 was reported in Yang et al. (2015). The ocean component of CESM1.0 is the Parallel Ocean Program version 2 (POP2; (Smith et al. 2010) and employs the gx1v6 curvilinear grid, comprising 384 × 320 grid points horizontally and 60 layers vertically. The zonal spacing within the ocean grid is uniformly set at 1.1258, while the meridional spacing varies non-uniformly: near the equator, the resolution is 0.278°, gradually increasing to a maximum of 0.65° at 60°N/S, and then tapering off toward the poles. Detailed configurations can be found in Yang et al. (2015). The simulation starts from a state of rest with the standard configuration for the preindustrial condition, and is integrated for 2500 years. For analysis, we use the data from the final 1900 years of the simulation.

In the CESM1.0 simulation, the mean salinity is 33.9 psu for the surface North Atlantic box and 33.7 psu for the surface South Atlantic box (Fig. A1a). The mean temperatures are 4.9 ℃ and 5.4 ℃ for the northern and southern boxes, respectively. The subtropic box, comprising regions of maximum surface salinity in the Atlantic, has mean salinity of 36.8 psu and mean temperature of 23.5 ℃. The mean AMOC is about 24 Sv.

Figure A1b shows the linear regression pattern of the AMOC index on the density anomalies over 4000-m depth. There is a strong positive (negative) correlation between the AMOC anomaly and the salinity anomaly in the subpolar North (South) Atlantic box. Figures A1c and d show the scattering plots of the AMOC anomaly versus the density difference between the North Atlantic and South Atlantic, and their time series. There is a strong positive, linear correlation between them, with a correlation coefficient of 0.89.

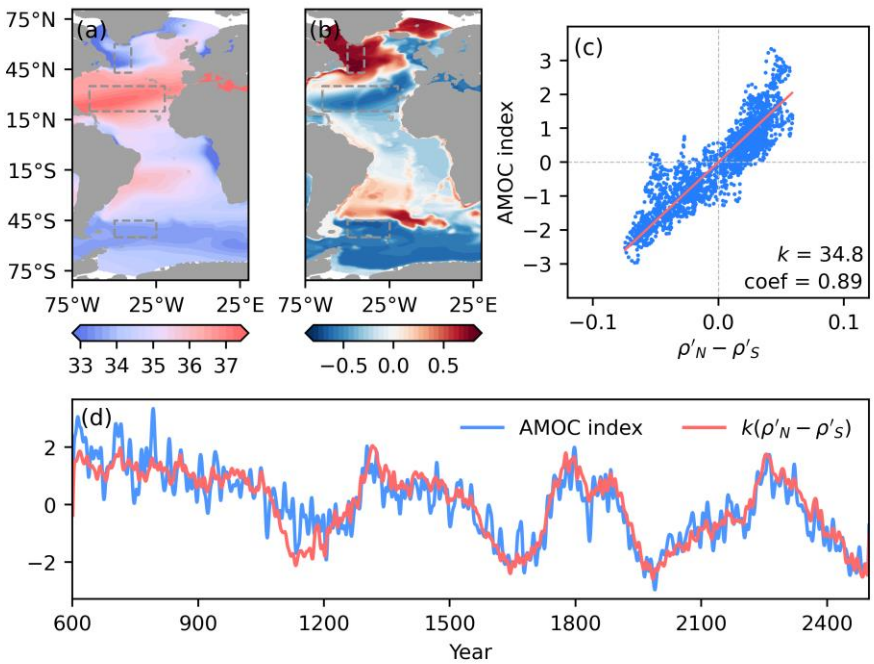

FIG. A1. (a) Climatology of sea-surface salinity (units: psu) in CESM 1.0. Dashed boxes outline the subpolar North, tropical, and subpolar South Atlantic boxes, respectively. (b) Regression of AMOC anomaly (units: Sv) on density anomaly integrated above 4000-m depth (units: kg m^{-3}). (c) Scatter plot of AMOC anomaly (ordinate) versus the difference of density anomaly (abscissa) averaged between the two regions in subpolar North and South Atlantic oceans, respectively. The red line represents the reduced major axis regression with a coefficient of 0.89 and a slope of 34.8 Sv kg^{-1} m^3. (d) Time series of AMOC anomaly (blue curve) and its estimation (red curve) from the reduced major axis regression. In (c) and (d), the anomalies of AMOC index and density are lowpass-filtered with a cutoff period of 10 years.

A 500-year simulation of the EC-Earth3-Veg-LR model output was obtained from the World Climate Research Program (WCRP) Coupled Model Intercomparison Project, Phase 6 (CMIP6) data, provided by the EC-Earth-Consortium team for the “pre-industrial control” (piControl) experiment. The ocean component of the model utilized version 3.6 of the Nucleus for European Modelling of the Ocean (NEMO3.6) in the ORCA1 configuration. This configuration uses a tripolar grid of poles, and comprises 362 x 292 horizontal grids and 75 vertical levels. The spatial resolution was predominantly set at 1 degree, with a refined resolution of 1/3 degrees in the tropics. Detailed information regarding the model and its configuration can be found in Döscher et al. (2022).

In the EC-Earth3-Veg-LR simulations, the mean salinity is 32.5 psu for the surface North Atlantic box and 33.7 psu for the surface South Atlantic box (Fig. A2a). The mean temperatures are 3.5 ℃ and 6.9 ℃ for the northern and southern boxes, respectively. The subtropic box has mean salinity of 36.7 psu and mean temperature of 22.7 ℃. The mean AMOC is about 18 Sv.

Figure A2b shows the linear regression pattern of the AMOC index on the density anomalies over 4000-m depth. Figures A2c and d show the scattering plots of the AMOC anomaly versus the density difference between the North Atlantic and South Atlantic, and their time series. There is also a strong positive, linear correlation between them, with a correlation coefficient of 0.81.

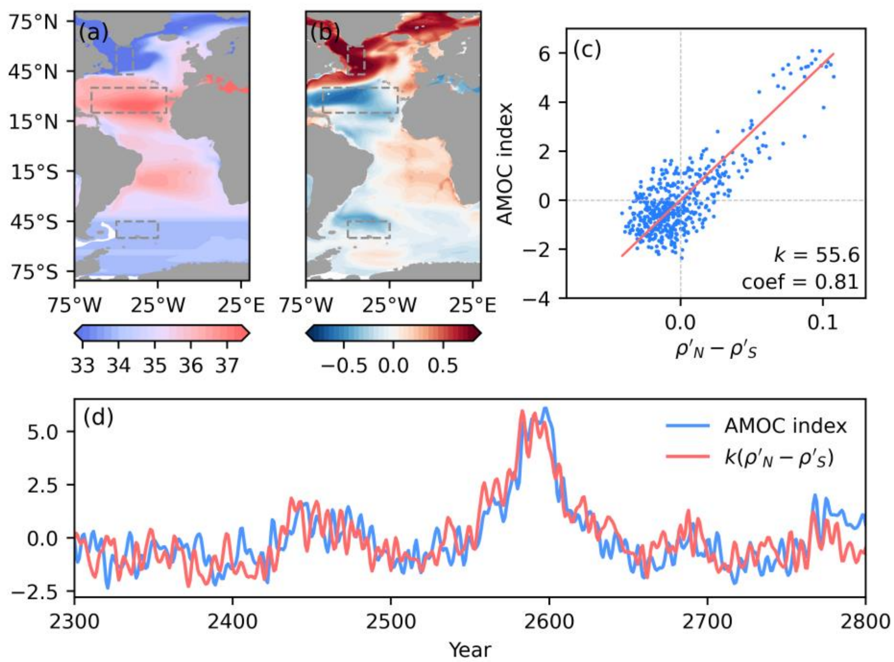

FIG. A2. Same as Fig. A1, but for EC-Earth3-Veg-LR simulation results. The regression coefficient in (b) is 0.81, and the slope is 55.6 Sv kg^{-1} m^3. The cutoff period for filtering in (d) is five years.

APPENDIX B

Theoretical solution to the multicentennial oscillatory mode

Similar to LY22, if we consider extreme mixing in the subpolar North Atlantic, the 6S model can be reduced to a 5-box model, namely the 5S model (Fig. B1a). Eq. (3) can be simplified as follows,

$$V_1\dot{S}_1' = \bar{q}(S_2' - S_1') + q'(\bar{S}_2 - \bar{S}_1) \tag{B1a}$$

$$V_2\dot{S}_2' = \bar{q}(S_3' - S_2') + q'(\bar{S}_3 - \bar{S}_2) \tag{B1b}$$

$$V_3\dot{S}_3' = \bar{q}(S_6' - S_3') + q'(\bar{S}_1 - \bar{S}_3) \tag{B1c}$$

$$V_5\dot{S}_5' = \bar{q}(S_1' - S_5') \tag{B1d}$$

$$V_6\dot{S}_6' = \bar{q}(S_5' - S_6') \tag{B1e}$$

In the 5S model, the eigenmode of the multicentennial oscillation is only slightly different from that in the 6S model (Fig. B2). This is similar to the case in the one-hemisphere box model (LY22).

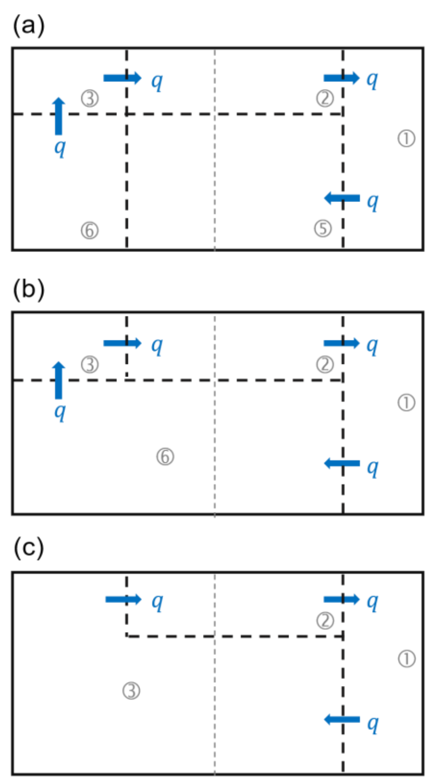

FIG. B1. Schematic diagrams of (a) 5-box model (5S model), and simplified (b) 4-box model (4S model), and (c) 3-box model (3S model). In the 5S model, the two subpolar North Atlantic boxes are merged, representing the enhanced mixing there. In the 4S model, the lower oceans in the equatorial and subpolar South Atlantic are combined into one box; in the 3S model, the whole subpolar South Atlantic is further merged with the equatorial lower oceans.

To solve the eigenvalues in the two-hemisphere box model, the 5S model can be further simplified to a 4-box model (namely the 4S model) by merging the deep ocean box at the equator and South Atlantic, and to a 3-box model (namely the 3S model) by further including the box of the upper South Atlantic, as shown in Fig. B1.

The equations of the 4S model are written as follows,

$$V_1\dot{S}_1' = \bar{q}(S_2' - S_1') + q'(\bar{S}_2 - \bar{S}_1) \tag{B2a}$$

$$V_2\dot{S}_2' = \bar{q}(S_3' - S_2') + q'(\bar{S}_3 - \bar{S}_2) \tag{B2b}$$

$$V_3\dot{S}_3' = \bar{q}(S_6' - S_3') + q'(\bar{S}_1 - \bar{S}_3) \tag{B2c}$$

$$V_6\dot{S}_6' = \bar{q}(S_1' - S_6') \tag{B2d}$$

The equations of the 3S model are written as follows,

$$V_1\dot{S}_1' = \bar{q}(S_2' - S_1') + q'(\bar{S}_2 - \bar{S}_1) \tag{B3a}$$

$$V_2\dot{S}_2' = \bar{q}(S_3' - S_2') + q'(\bar{S}_3 - \bar{S}_2) \tag{B3b}$$

$$V_3\dot{S}_3' = \bar{q}(S_1' - S_3') + q'(\bar{S}_1 - \bar{S}_3) \tag{B3c}$$

Similar to the 6S model, the difference of equilibrium salinity in the 3S model is related to the surface freshwater flux, which is given by,

$$F_{w1} = \bar{q}(\bar{S}_1 - \bar{S}_2) \tag{B4a}$$

$$F_{w2} = \bar{q}(\bar{S}_2 - \bar{S}_3) \tag{B4b}$$

$$F_{w3} = \bar{q}(\bar{S}_3 - \bar{S}_1) \tag{B4c}$$

The eigenvalues of the 3S, 4S, 5S, and 6S models are very similar (Fig. B2). The minimum periods for the 3S, 4S, 5S, and 6S models are about 330, 330, 350, and 340 years, respectively, which indicates that the simplification does not change the fundamentals of the multicentennial oscillation.

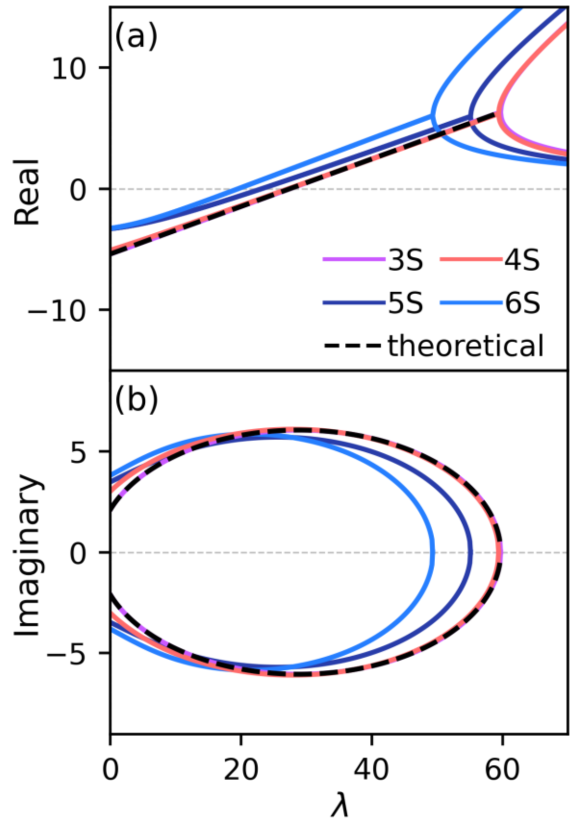

FIG. B2. Dependences of (c) real and (d) imaginary parts of the multicentennial oscillatory modes on λ in the 3S, 4S, 5S, and 6S, respectively. Dashed black curve represents the theoretical solution to the 3S model. The units of the ordinate are 10^{-10} s^{-1}. The parameters take the values in Table 1.

The 3S model can be solved analytically. By subtracting Eq. (B3a) from Eq. (B3b) and Eq. (B3c), respectively, we obtain,

$$\dot{a}' = (-\sigma_1\bar{q} - \sigma_2\bar{q})a' + (M_{sn}\lambda - M_{ss}\lambda + \sigma_2\bar{q})h' \tag{B5a}$$

$$\dot{h}' = (-\sigma_1\bar{q})a' + (M_{sn}\lambda - M_{s}\lambda - \sigma_3\bar{q})h' \tag{B5b}$$

where $M_{sn} = \rho_0\beta\frac{\overline{S_2}-\overline{S_1}}{V_1}$, $M_{ss} = \rho_0\beta\frac{\overline{S_3}-\overline{S_2}}{V_2}$, $M_s = \rho_0\beta\frac{\overline{S_1}-\overline{S_3}}{V_3}$, $\sigma_1 = \frac{1}{V_1}$, $\sigma_2 = \frac{1}{V_2}$, and $\sigma_3 = \frac{1}{V_3}$.

Hence, we can define the following quantities:

$$C_1 = -(\sigma_1 + \sigma_2)\bar{q}$$

$$C_2 = (M_{sn} - M_{ss})\lambda + \sigma_2\bar{q}$$

$$C_3 = -\sigma_1\bar{q}$$

$$C_4 = (M_{sn} - M_s)\lambda - \sigma_3\bar{q}$$

Assuming the form of solution as $a' = Ae^{\omega t}$, Eq. (A5) has eigenvalues as follows,

$$\omega = \frac{1}{2}\left[(C_1 + C_4) \pm \sqrt{(C_1 + C_4)^2 - 4(C_1C_4 - C_2C_3)}\right] \tag{B6}$$

If $\Delta = (C_1 + C_4)^2 - 4(C_1C_4 - C_2C_3) < 0$, we have oscillatory solutions, which are,

$$\mathrm{Re}(\omega) = \frac{1}{2}(C_1 + C_4) \tag{B7a}$$

$$\mathrm{Im}(\omega) = \frac{1}{2}(\sqrt{4(C_1C_4 - C_2C_3) - (C_1 + C_4)^2}) \tag{B7b}$$

Eqs. (B6) and (B7) give the theoretical eigenmodes of the 3S model (black curves in Fig. B2a, b), which are consistent with the numerical results.

The period of the oscillation (Δ) lies on the imaginary part of the eigenvalue, which can be rewritten as follows,

$$\begin{aligned}\Delta &= 4(C_1C_4 - C_2C_3) - (C_1 + C_4)^2 \\ &= -(C_1 - C_4)^2 - 4C_2C_3 \\ &= -(M_{sn}\lambda - M_s\lambda - \sigma_3\bar{q} + \sigma_1\bar{q} + \sigma_2\bar{q})^2 + 4\sigma_1\bar{q}(M_{sn}\lambda - M_{ss}\lambda + \sigma_2\bar{q}) \\ &= -(M_{sn} - M_s)^2\lambda^2 - (\sigma_1 + \sigma_2 - \sigma_3)^2\bar{q}^2 + 4\sigma_1\sigma_2\bar{q}^2 \\ &\quad -2\bar{q}(M_{sn} - M_s)(\sigma_1 + \sigma_2 - \sigma_3)\lambda + 4\sigma_1\bar{q}(M_{sn} - M_{ss})\lambda\end{aligned} \tag{B8}$$

(B8) suggests that the surface freshwater flux and λ interact to influence the period of the multicentennial oscillation. In other words, the specific value of λ can determine the extent to which the surface freshwater flux impacts the period.

Δ is a quadratic function of λ and has a maximum occurring at,

$$\begin{aligned}\lambda = \lambda_{max} &= -\frac{-2\bar{q}(M_{sn} - M_s)(\sigma_1 + \sigma_2 - \sigma_3) + 4\sigma_1\bar{q}(M_{sn} - M_{ss})}{-2(M_{sn} - M_s)^2} \\ &= \frac{-\bar{q}(M_{sn} - M_s)(\sigma_1 + \sigma_2 - \sigma_3) + 2\sigma_1\bar{q}(M_{sn} - M_{ss})}{(M_{sn} - M_s)^2}\end{aligned} \tag{B9}$$

The maximum Δ is determined by,

$$\begin{aligned}\Delta_{max} &= -(\sigma_1+\sigma_2-\sigma_3)^2\bar{q}^2 + 4\sigma_1\sigma_2\bar{q}^2 + \frac{[2\bar{q}(M_{sn}-M_s)(\sigma_1+\sigma_2-\sigma_3) - 4\sigma_1\bar{q}(M_{sn}-M_{ss})]^2}{4(M_{sn}-M_s)^2} \\ &= -(\sigma_1+\sigma_2-\sigma_3)^2\bar{q}^2 + 4\sigma_1\sigma_2\bar{q}^2 + \left[(\sigma_1+\sigma_2-\sigma_3) - 2\sigma_1\frac{M_{sn}-M_{ss}}{M_{sn}-M_s}\right]^2\bar{q}^2 \\ &= -\bar{q}^2[(\sigma_1+\sigma_2-\sigma_3)^2 - 4\sigma_1\sigma_2 - (\sigma_1+\sigma_2-\sigma_3-2\sigma_1 M)^2] \\ &= -\bar{q}^2[-4\sigma_1\sigma_2 - 4{\sigma_1}^2M^2 + 4\sigma_1 M(\sigma_1+\sigma_2-\sigma_3)] \\ &= 4\sigma_1\sigma_2\bar{q}^2\left[1+\frac{\sigma_1}{\sigma_2}M^2 - \frac{1}{\sigma_2}M(\sigma_1+\sigma_2-\sigma_3)\right] \\ &= 4\sigma_1\sigma_2\bar{q}^2\left[1+\frac{\sigma_1}{\sigma_2}M^2 - \left(\frac{\sigma_1}{\sigma_2}+1-\frac{\sigma_3}{\sigma_2}\right)M\right] \end{aligned} \tag{B10}$$

where $M = \frac{M_{sn}-M_{ss}}{M_{sn}-M_s} = \frac{\frac{1}{V_1}(\overline{S_2}-\overline{S_1}) - \frac{1}{V_2}(\overline{S_3}-\overline{S_2})}{\frac{1}{V_1}(\overline{S_2}-\overline{S_1}) - \frac{1}{V_3}(\overline{S_1}-\overline{S_3})} = \frac{\frac{F_{W1}}{V_1}-\frac{F_{W2}}{V_2}}{\frac{F_{W1}}{V_1}-\frac{F_{W3}}{V_3}} = \frac{V_3}{V_2}\left(\frac{V_2F_{W1}-V_1F_{W2}}{V_3F_{W1}-V_1F_{W3}}\right)$.

Thus, the theoretical solution to the 3S model gives the minimum period of the multicentennial oscillatory mode as follows,

$$\begin{aligned}T_{min} &= \frac{2\pi}{\frac{1}{2}\sqrt{\Delta_{max}}} = \frac{2\pi}{\bar{q}}\frac{1}{\sqrt{\sigma_1\sigma_2}}\frac{1}{\sqrt{1+\frac{\sigma_1}{\sigma_2}M^2-\left(\frac{\sigma_1}{\sigma_2}+1-\frac{\sigma_3}{\sigma_2}\right)M}} \\ &= \frac{2\pi\sqrt{V_1V_2}}{\bar{q}}\frac{1}{\sqrt{1+\frac{V_2}{V_1}M^2-\left(\frac{V_2}{V_1}-\frac{V_2}{V_3}+1\right)M}}\end{aligned} \tag{B11}$$

In M, $\frac{1}{V_1}(\overline{S_2}-\overline{S_1})$, $\frac{1}{V_2}(\overline{S_3}-\overline{S_2})$, and $\frac{1}{V_3}(\overline{S_1}-\overline{S_3})$ represent the relative contribution of perturbation advection (i.e., $q'(\overline{S_2}-\overline{S_1})$, $q'(\overline{S_3}-\overline{S_2})$, and $q'(\overline{S_1}-\overline{S_3})$) to S_1', S_2', and S_3'. Hence, the physics of M is the relative contribution of perturbation advection to $\frac{S_1'-S_2'}{S_1'-S_3'}$, which is positively correlated with $\frac{-\bar{q}(S_2'-S_1')}{q'(\overline{S_2}-\overline{S_1})}$ and $\frac{-\bar{q}(S_2'-S_1')}{q'(\overline{S_1}-\overline{S_3})}$, the specific values of the negative mean advection and positive perturbation advection feedbacks. This result suggests that when mean advection dominates, stronger negative feedback of mean advection and weaker (stronger) positive perturbation advection feedback shorten the period; when perturbation advection feedback dominates, the same change can lengthen the period.

Mathematically, a damped oscillation in the 3-box model can exist when Re(ω) < 0. Therefore, the stability criterion can be expressed as follows,

$$\lambda < \lambda_C \equiv (\sigma_1+\sigma_2+\sigma_3)\frac{\bar{q}}{M_{sn}-M_s} \tag{B12}$$

When $\lambda = \lambda_C$, Re(ω) = 0. The period of the undamped oscillation is given by,

$$\begin{aligned}\Delta_C &= -4\left({C_1}^2 + C_2C_3\right) = -4[(\sigma_1+\sigma_2)^2\bar{q}^2 - \sigma_1\bar{q}(M_{sn}-M_{ss})\lambda_C - \sigma_1\sigma_2\bar{q}^2] \\ &= -4\bar{q}^2[(\sigma_1+\sigma_2)^2 - \sigma_1(\sigma_1+\sigma_2+\sigma_3)M - \sigma_1\sigma_2]\end{aligned} \tag{B13a}$$

$$T_C = \frac{2\pi}{\frac{1}{2}\sqrt{\Delta_C}} = \frac{2\pi}{\bar{q}}\frac{1}{\sqrt{\sigma_1(\sigma_1+\sigma_2+\sigma_3)M + \sigma_1\sigma_2 - (\sigma_1+\sigma_2)^2}} \tag{B13b}$$

There is a relationship between λ_{max}, λ_C and M, that is,

$$\frac{\lambda_{max}}{\lambda_C} = \frac{-(M_{sn}-M_s)(\sigma_1+\sigma_2-\sigma_3) + 2\sigma_1(M_{sn}-M_{ss})}{(\sigma_1+\sigma_2+\sigma_3)(M_{sn}-M_s)} = \frac{-(\sigma_1+\sigma_2-\sigma_3)+2\sigma_1 M}{\sigma_1+\sigma_2+\sigma_3} \tag{B14}$$

Therefore, the minimum period and critical period can be written as follows,

$$\begin{aligned}T_{min} &= \frac{2\pi}{\frac{1}{2}\sqrt{\Delta_{max}}} = \frac{2\pi}{\bar{q}}\frac{1}{\sqrt{\sigma_1\sigma_2}}\frac{1}{\sqrt{1 - \frac{(\sigma_1+\sigma_2-\sigma_3)^2}{4\sigma_1\sigma_2} + \frac{(\sigma_1+\sigma_2+\sigma_3)^2}{4\sigma_1\sigma_2}\frac{{\lambda_{max}}^2}{{\lambda_C}^2}}} \\ &= \frac{2\pi\sqrt{V_1V_2}}{\bar{q}}\frac{1}{\sqrt{1 - \frac{(V_2V_3+V_1V_3-V_1V_2)^2}{4V_1V_2{V_3}^2} + \frac{(V_2V_3+V_1V_3+V_1V_2)^2}{4V_1V_2{V_3}^2}\frac{{\lambda_{max}}^2}{{\lambda_C}^2}}}\end{aligned} \tag{B15a}$$

$$\begin{aligned}T_C &= \frac{2\pi}{\frac{1}{2}\sqrt{\Delta_C}} = \frac{2\pi}{\bar{q}}\frac{1}{\sqrt{\frac{\lambda_{max}}{\lambda_C}\frac{(\sigma_1+\sigma_2+\sigma_3)^2}{2} - \frac{{\sigma_1}^2+{\sigma_2}^2+{\sigma_3}^2}{2}}} \\ &= \frac{2\pi}{\bar{q}}\frac{1}{\sqrt{\frac{\lambda_{max}}{\lambda_C}\frac{(V_2V_3+V_1V_3+V_1V_2)^2}{2{V_1}^2{V_2}^2{V_3}^2} - \frac{{V_2}^2{V_3}^2+{V_1}^2{V_3}^2+{V_1}^2{V_2}^2}{2{V_1}^2{V_2}^2{V_3}^2}}}\end{aligned} \tag{B15b}$$

Eq. (B15) indicates that both the minimum period and critical period depend on basin geometry, mean AMOC strength, and the specific ratio of λ_{max}: λ_C. In the theoretical solution, the ratio has a relationship with M [Eq. (B14)], a function of surface freshwater flux. However, in the real world, the ratio can be more flexible and be affected by other processes of the climate system.

If we let F_{w2} = 0 and F_{w1} + F_{w3} = 0, we will have $\overline{S_2}$ = $\overline{S_3}$ and

$$M = \frac{V_3}{V_1+V_3} \tag{B16a}$$

The theoretical solution of the period becomes,

$$T = \frac{2\pi}{\bar{q}}\sqrt{\frac{V_1V_2}{\frac{V_1V}{(V_1+V_3)^2}}} = \frac{2\pi(V_1+V_3)}{\bar{q}}\sqrt{\frac{V_2}{V_1+V_2+V_3}} \tag{B16b}$$

If we let F_{w3} = 0 and F_{w1} + F_{w2} = 0, we will have $\overline{S_1} = \overline{S_3}$ and

$$M = 1 + \frac{V_1}{V_2} \tag{B17a}$$

The theoretical solution of the period becomes,

$$T = \frac{2\pi}{\bar{q}}\sqrt{\frac{V_1V_2}{\frac{V}{V_3}}} = \frac{2\pi}{\bar{q}}\sqrt{\frac{V_1V_2V_3}{V_1+V_2+V_3}} \tag{B17b}$$

When F_{w3} = 0, we also obtain $\lambda_{max} = \lambda_C$, which may be very similar to the condition in the real world.

Eqs. (B16) and (B17) indicate that when the freshwater flux of the equatorial or South Atlantic Ocean is set to zero (i.e., $F_{w2} = 0$ or $F_{w3} = 0$), the solutions of minimum period become unrelated to the surface freshwater flux and depend only on the basin geometry and AMOC strength. This result is consistent with that in LY22 where the freshwater flux in the equatorial ocean is equal to that in the North Atlantic.

REFERENCES

Askjær, T. G., and Coauthors, 2022: Multi-centennial Holocene climate variability in proxy records and transient model simulations. *Quat. Sci. Rev.*, **296,** 107801, 10.1016/j.quascirev.2022.107801.

Bond, G., and Coauthors, 1997: A pervasive millennial-scale cycle in North Atlantic Holocene and glacial climates. *Science*, **278,** 1257-1266, 10.1126/science.278.5341.1257.

Burls, N. J., A. V. Fedorov, D. M. Sigman, S. L. Jaccard, R. Tiedemann, and G. H. Haug, 2017: Active Pacific meridional overturning circulation (PMOC) during the warm Pliocene. *Science Advances*, **3,** e1700156, 10.1126/sciadv.1700156.

Cao, N., Q. Zhang, K. E. Power, F. Schenk, K. Wyser, and H. Yang, 2023: The role of internal feedbacks in sustaining multi-centennial variability of the Atlantic Meridional Overturning Circulation revealed by EC-Earth3-LR simulations. *Earth and Planetary Science Letters*, **621,** 118372

Dansgaard, W., S. Johnsen, H. Clausen, D. Dahl ‐ Jensen, N. Gundestrup, C. Hammer, and H. Oeschger, 1984: North Atlantic climatic oscillations revealed by deep Greenland ice cores. *Climate processes and climate sensitivity*, **29,** 288-298

Delworth, T. L., and F. Zeng, 2012: Multicentennial variability of the Atlantic meridional overturning circulation and its climatic influence in a 4000 year simulation of the GFDL CM2.1 climate model. *Geophys. Res. Lett.*, **39**, 10.1029/2012gl052107.

Döscher, R., and Coauthors, 2022: The EC-Earth3 Earth system model for the Coupled Model Intercomparison Project 6. *Geoscientific Model Development*, **15,** 2973-3020, 10.5194/gmd-15-2973-2022.

Gao, Y.-Q., and L. Yu, 2008: Subpolar Gyre Index and the North Atlantic Meridional Overturning Circulation in a Coupled Climate Model. *Atmos. Ocean. Sci. Lett.*, **1,** 29-32, 10.1080/16742834.2008.11446764.

Griesel, A., and M. A. M. Maqueda, 2006: The relation of meridional pressure gradients to North Atlantic deep water volume transport in an ocean general circulation model. *Climate Dyn.*, **26,** 781-799, 10.1007/s00382-006-0122-z.

Griffies, S. M., and E. Tziperman, 1995: A linear thermohaline oscillator driven by stochastic atmospheric forcing. *J. Climate*, **8,** 2440-2453, 10.1175/1520-0442(1995)008<2440:ALTODB>2.0.CO;2.

Guan, Y. P., and R. X. Huang, 2008: Stommel's box model of thermohaline circulation revisited—The role of mechanical energy supporting mixing and the wind-driven gyration. *J. Phys. Oceanogr.*, **38,** 909-917, 10.1175/2007JPO3535.1.

Hughes, T. M. C., and A. J. Weaver, 1994: Multiple Equilibria of an Asymmetric Two-Basin Ocean Model. *J. Phys. Oceanogr.*, **24,** 619-637, 10.1175/1520-0485(1994)024<0619:meoaat>2.0.co;2.

Jiang, W., G. Gastineau, and F. Codron, 2021: Multicentennial variability driven by salinity exchanges between the Atlantic and the Arctic Ocean in a coupled climate model. *J. Adv. Model. Earth Syst.*, **13,** e2020MS002366, 10.1029/2020MS002366.

Klockmann, M., U. Mikolajewicz, H. Kleppin, and J. Marotzke, 2020: Coupling of the Subpolar Gyre and the Overturning Circulation During Abrupt Glacial Climate Transitions. *Geophys. Res. Lett.*, **47**, 10.1029/2020gl090361.

Li, Y., and H. Yang, 2022: A Theory for Self-Sustained Multicentennial Oscillation of the Atlantic Meridional Overturning Circulation. *J. Climate*, **35,** 5883-5896, 10.1175/jcli-d-21-0685.1.

Lucarini, V., and P. H. Stone, 2005a: Thermohaline circulation stability: A box model study. Part I: Uncoupled model. *J. Climate*, **18,** 501-513, 10.1175/JCLI-3278.1.

——, 2005b: Thermohaline circulation stability: a box model study. Part II: coupled atmosphere–ocean model. *J. Climate*, **18,** 514-529, 10.1175/JCLI-3279.1.

Martin, T., W. Park, and M. Latif, 2013: Multi-centennial variability controlled by Southern Ocean convection in the Kiel Climate Model. *Climate Dyn.*, **40,** 2005-2022, 10.1007/s00382-012-1586-7.

——, 2015: Southern Ocean forcing of the North Atlantic at multi-centennial time scales in the Kiel Climate Model. *Deep Sea Res., Part II*, **114,** 39-48, 10.1016/j.dsr2.2014.01.018.

McCreary, J. P., and P. Lu, 1994: Interaction between the subtropical and equatorial ocean circulations: The subtropical cell. *J. Phys. Oceanogr.*, **24,** 466-497

Meccia, V. L., R. Fuentes-Franco, P. Davini, K. Bellomo, F. Fabiano, S. Yang, and J. Von Hardenberg, 2022: Internal multi-centennial variability of the Atlantic Meridional Overturning Circulation simulated by EC-Earth3. *Climate Dyn.*, 10.1007/s00382-022-06534-4.

Mehling, O., K. Bellomo, M. Angeloni, C. Pasquero, and J. Von Hardenberg, 2023: High-latitude precipitation as a driver of multicentennial variability of the AMOC in a climate model of intermediate complexity. *Climate Dyn.*, **61,** 1519-1534, 10.1007/s00382-022-06640-3.

Mikolajewicz, U., and E. Maier-Reimer, 1990: Internal secular variability in an ocean general circulation model. *Climate Dyn.*, **4,** 145-156, 10.1007/BF00209518.

Moffa‐Sánchez, P., and Coauthors, 2019: Variability in the Northern North Atlantic and Arctic Oceans Across the Last Two Millennia: A Review. *Paleoceanogr. Paleoclimatology.*, **34,** 1399-1436, 10.1029/2018pa003508.

Mysak, L., T. Stocker, and F. Huang, 1993: Century-scale variability in a randomly forced, two-dimensional thermohaline ocean circulation model. *Climate Dyn.*, **8,** 103-116

Okazaki, Y., and Coauthors, 2010: Deepwater formation in the North Pacific during the last glacial termination. *Science*, **329,** 200-204

Park, W., and M. Latif, 2008: Multidecadal and multicentennial variability of the meridional overturning circulation. *Geophys. Res. Lett.*, **35**, 10.1029/2008gl035779.

Pasquero, C., and E. Tziperman, 2004: Effects of a Wind-Driven Gyre on Thermohaline Circulation Variability. *J. Phys. Oceanogr.*, **34,** 805-816, 10.1175/1520-0485(2004)034<0805:eoawgo>2.0.co;2.

Rahmstorf, S., 1996: On the freshwater forcing and transport of the Atlantic thermohaline circulation. *Climate Dyn.*, **12,** 799-811, 10.1007/s003820050144.

Rivin, I., and E. Tziperman, 1997: Linear versus Self-Sustained Interdecadal Thermohaline Variability in a Coupled Box Model. *J. Phys. Oceanogr.*, **27,** 1216-1232, 10.1175/1520-0485(1997)027<1216:Lvssit>2.0.Co;2.

Schott, F. A., J. P. McCreary Jr, and G. C. Johnson, 2004: Shallow overturning circulations of the tropical-subtropical oceans. *Washington DC American Geophysical Union Geophysical Monograph Series*, **147,** 261-304

Scott, J. R., J. Marotzke, and P. H. Stone, 1999: Interhemispheric thermohaline circulation in a coupled box model. *J. Phys. Oceanogr.*, **29,** 351-365, 10.1175/1520-0485(1999)029<0351:ITCIAC>2.0.CO;2.

Sejrup, H. P., H. Haflidason, and J. T. Andrews, 2011: A Holocene North Atlantic SST record and regional climate variability. *Quat. Sci. Rev.*, **30,** 3181-3195, 10.1016/j.quascirev.2011.07.025.

Sévellec, F., T. Huck, and M. Ben Jelloul, 2006: On the mechanism of centennial thermohaline oscillations. *J. Mar. Res.*, **64,** 355-392, 10.1357/002224006778189608.

Smith, R., and Coauthors, 2010: The parallel ocean program (POP) reference manual ocean component of the community climate system model (CCSM) and community earth system model (CESM). *LAUR-01853*, **141,** 1-140

Srokosz, M., and Coauthors, 2012: Past, Present, and Future Changes in the Atlantic Meridional Overturning Circulation. *Bull. Amer. Meteor. Soc.*, **93,** 1663-1676, 10.1175/bams-d-11-00151.1.

Stocker, T. F., and L. A. Mysak, 1992: Climatic fluctuations on the century time scale: A review of high-resolution proxy data and possible mechanisms. *Clim. Change*, **20,** 227-250, 10.1007/BF00139840.

Sun, J., M. Latif, and W. Park, 2021: Subpolar Gyre – AMOC – Atmosphere Interactions on Multidecadal Timescales in a Version of the Kiel Climate Model. *J. Climate*, 1-56, 10.1175/jcli-d-20-0725.1.

te Raa, L. A., and H. A. Dijkstra, 2003: Modes of internal thermohaline variability in a single-hemispheric ocean basin. *J. Mar. Res.*, **61,** 491-516

Thorpe, R. B., J. M. Gregory, T. C. Johns, R. A. Wood, and J. F. B. Mitchell, 2001: Mechanisms Determining the Atlantic Thermohaline Circulation Response to Greenhouse Gas Forcing in a Non-Flux-Adjusted Coupled Climate Model. *J. Climate*, **14,** 3102-3116, 10.1175/1520-0442(2001)014<3102:MDTATC>2.0.CO;2.

Treguier, A. M., and Coauthors, 2014: Meridional transport of salt in the global ocean from an eddy-resolving model. *Ocean Sci.*, **10,** 243-255, 10.5194/os-10-243-2014.

Vallis, G. K., 2017: *Atmospheric and oceanic fluid dynamics.* Cambridge University Press. https://doi.org/10.1017/9781107588417

Vallis, G. K., and R. Farneti, 2009: Meridional energy transport in the coupled atmosphere-ocean system: scaling and numerical experiments. *Quart. J. Roy. Meteor. Soc.*, **135,** 1643-1660, 10.1002/qj.498.

Wanner, H., and Coauthors, 2008: Mid- to Late Holocene climate change: an overview. *Quat. Sci. Rev.*, **27,** 1791-1828, 10.1016/j.quascirev.2008.06.013.

Weber, S., T. Crowley, and G. Van der Schrier, 2004: Solar irradiance forcing of centennial climate variability during the Holocene. *Climate Dyn.*, **22,** 539-553, 10.1007/s00382-004-0396-y.

Wei, X., and R. Zhang, 2022: A Simple Conceptual Model for the Self‐Sustained Multidecadal AMOC Variability. *Geophys. Res. Lett.*, **49**, 10.1029/2022gl099800.

Winton, M., and E. S. Sarachik, 1993: Thermohaline oscillations induced by strong steady salinity forcing of ocean general circulation models. *J. Phys. Oceanogr.*, **23,** 1389-1410, 10.1175/1520-0485(1993)023<1389:TOIBSS>2.0.CO;2.

Wood, R. A., J. M. Rodríguez, R. S. Smith, L. C. Jackson, and E. Hawkins, 2019: Observable, low-order dynamical controls on thresholds of the Atlantic meridional overturning circulation. *Climate Dyn.*, **53,** 6815-6834, 10.1007/s00382-019-04956-1.

Yang, H., Q. Li, K. Wang, Y. Sun, and D. Sun, 2015: Decomposing the meridional heat transport in the climate system. *Climate Dyn.*, **44,** 2751-2768, 10.1007/s00382-014-2380-5.

Yang, K., H. Yang, and Y. Li, 2024: A Theory for Self-sustained Multicentennial Oscillation of the Atlantic Meridional Overturning Circulation. Part II: Role of Temperature. *J. Climate*, **37,** 2787-2807, 10.1175/JCLI-D-22-0755.1.